ACS OMEGA

Open Access

http://pubs.acs.org/journal/acsodf

Article

Enhanced Catalytic Activity of a Copper(II) Metal–Organic Framework Constructed *via* Semireversible Single-Crystal-to-Single-Crystal Dehydration

Siya T. Hulushe,* Gareth M. Watkins, and Setshaba D. Khanye

Cite This: *ACS Omega* 2024, 9, 7511–7528

Read Online

ACCESS | Metrics & More | Article Recommendations | Supporting Information

ABSTRACT: Herein, we present a copper(II) metal–organic framework, $[Cu_2(btec)(OH_2)_4]\cdot 2H_2O$ (**1**) [$(btec)^{4-}$ = 1,2,4,5-benzenetetracarboxylate], that undergoes single-crystal-to-single-crystal transformations into two anhydrous phases **2′** and **2″** with the chemical formula $[Cu_2(btec)]$, triggered by two-step dehydration at 403 and 433 K, respectively. After immersion in water for 3 days at room temperature, **2′** transformed into $[Cu_2(btec)(OH_2)]$ (**3**), while both **2′** and **2″** took 1 week to revert to **1**. Dynamic vapor sorption studies validated water-induced reversible structural transformations at 70% relative humidity (RH). According to single-crystal X-ray diffraction (SC-XRD), the local coordination geometry of the Cu^{2+} ion in **2′** changed from a saturated octahedron to a coordinatively unsaturated square-based pyramid in **3**, manifested by changes in color and dimensionality. From a topological point of view, all of the scaffolds show a binodal (3,6)-connected **kgd** topology with the point symbol $\{4^3\}_2\{4^6\}$. In addition, the materials were thoroughly characterized using routine spectroscopic data and various analytical techniques. The catalytic activity of the microporous materials in the liquid-phase oxidation of styrene in acetonitrile, using 30% (wt) H_2O_2 as the oxidant, was investigated. The excellent performance of the monohydrous phase **3** was shown to be superior to the pristine framework and the anhydrous counterparts, as evidenced by a good turnover number (TON) and turnover frequency (TOF) = 82.6 and 21.0 h^{-1}, respectively. Within 4 h, the substrates were catalytically oxidized to the desired products with up to 67% conversion and 100% benzaldehyde selectivity. It is worth noting that the accessible active metal sites and higher surface area enhanced the catalytic properties of **3**. Furthermore, the maintenance of catalytic efficiency over five cycles and reusability are illustrated and discussed in terms of the structural differences of the microporous frameworks. Thus, a preliminary reaction mechanism for the selective oxidation of styrene is proposed. This study not only provides a fascinating example of MOF chromism achieved by thermal activation and rehydration but also sheds some light on the relationship between pore-surface- or metal-engineered sites in MOFs and their heterogeneous catalytic performances.

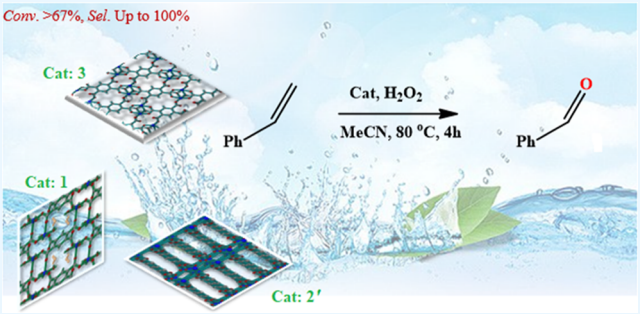

1. INTRODUCTION

Metal–organic frameworks (MOFs) are an emerging class of crystalline materials composed of inorganic vertices (metal nodes or clusters) coordinated with organic struts (spacers) to form one-dimensional (1D), two-dimensional (2D), or three-dimensional (3D) architectures.[1,2] MOFs are widely regarded as a subtype of coordination polymers or coordination frameworks. Essentially, MOFs consist of open channels formed primarily by ejecting guest and terminal coordinated solvents through low-pressure heating.[3,4] Of the numerous porous materials reported to date, only a handful of examples show a much greater range of response to external stimuli than conventional materials.[5,6] Moreover, the activation of MOFs, which raises the energy state of these materials by eliminating the pore-filling solvent in the pore channels and the coordinating solvent that saturates the metal nodes, is an essential prerequisite for the use of MOFs in a variety of important structural applications,[7−9] ranging from luminescence to molecular magnetism,[10,11] gas storage,[12] gas or liquid separation,[13] drug delivery,[14] photocatalysis,[15] electrocatalysis,[16,17] etc. Another industrially relevant application for which MOFs have shown promise is heterogeneous catalysis,[18,19] which is proving to be a versatile alternative to conventional inorganic materials, especially for a variety of organic oxidation processes.

MOF-based catalysts rely not only on the open metal sites and permanent porosity of the framework but also on other

Received: August 18, 2023
Revised: December 15, 2023
Accepted: January 5, 2024
Published: February 12, 2024

https://doi.org/10.1021/acsomega.3c05999
ACS Omega 2024, 9, 7511–7528

properties such as reversible structural transformation[20] (or reproducibility) that ideally occurs in the single-crystal-to-single-crystal (SCSC) fashion. Most SCSC transitions are triggered by temperature,[21] light,[22] and removal of guest molecules, especially solvents,[23] which often lead to catastrophic structural collapse of the host matrix.[24,25] However, the SCSC transformation of MOFs remains a challenge, owing to the difficulty of cleaving and establishing chemical bonds in more than one direction in the solid state. Many MOFs lose their crystallinity during the transition process. Until now, the majority of these SCSC transformations have been based on postsynthetic modification of organic linkers or metal ions exchanging in inorganic nodes, with only few of these transitions involving changes of the coordination bonds and pore aperture rearrangement being reported.[26] The SCSC transformation is particularly intriguing because it enables direct visualization of the crystal structure change as it occurs during the transformation process.[27] Furthermore, it may be beneficial for an understanding of the dynamics of the system as well as the processes that contribute to SCSC transitions. In general, the development of materials with adaptive crystal lattices capable of large phase transitions remains a major challenge. SCSC structural transformations of MOFs with recoverable property changes, on the other hand, can lead to the development of innovative functional materials.[28] For example, solid-state reactivity *via* thermal dehydration of $[Cu_2(bpa)(btec)(OH_2)_4]$ to $[Cu_2(bpa)(btec)]$ (bpa = 1,2-bis(4-pyridyl)ethane, $(btec)^{4-}$ = 1,2,4,5-benzenetetracarboxylate) resulted in a novel framework with improved thermal stability.[29] This reversible phase transformation, triggered by the gradual removal of coordinating water molecules, is also associated with solvatochromism.[30,31] In 2009, Spodine and colleagues used an anhydrous Cu(II)-based MOF $[Cu_2(bipy)_2(btec)]$ (bipy = 2,2′-bipyridine) as a heterogeneous catalyst for styrene oxidation.[32] In the presence of *tert*-butyl hydroperoxide (*t*-BuOOH), this material affords a mixture of benzaldehyde and styrene oxide with a turnover number (TON) of 673 and a turnover frequency (TOF) of 28 h^{-1}.[32] Interestingly, selective oxidation of styrene to benzaldehyde with a conversion of 37% (TOF = 25 h^{-1}) was detected over the same anhydrous Cu(II) framework when *t*-BuOOH was replaced by 30% (wt) aqueous hydrogen peroxide (H_2O_2) in a water−dichloroethane or *n*-decane medium.[31,32] However, the limited porosity of $[Cu_2(bipy)_2(btec)]$ is a significant drawback in its use as a catalyst.

In the ongoing investigation of porous networks, copper-based MOFs have piqued our interest since Cu(II) atoms possess a range of coordination geometries such as tetrahedral (T_d), square-planar (SQP), trigonal bipyramidal (TBP), square-based pyramidal (SBP), and octahedral (O_h). In this study, we report the synthesis and characterization of a 2D coordination framework with SBP geometry, namely, $\mathbf{[Cu_2(btec)(OH_2)_4]\cdot 2H_2O}$ (**1**). Furthermore, we describe two new anhydrous MOF forms, **2′** and **2″** (with chemical formula $\mathbf{[Cu_2(btec)]}$), both prepared from as-synthesized **1** *via* temperature-controlled SCSC phase transformations. The reproducibility of such transitions was also investigated. After 3 days of hydration at room temperature (RT), **2′** converted to **3**, while **1** retained its original structure after 1 week of water immersion. This allowed us to study these massive structural transformations at the atomic level using single-crystal X-ray diffraction analysis (SC-XRD). X-ray structure determination shows that $\mathbf{[Cu_2(btec)(OH_2)]}$ (**3**) is a novel 2D polymeric structure possessing open copper active sites with SBP geometry, adopting (3,6)-connected Kagomé-dual (**kgd**) topology, while **2′** and **2″** are both 3D networks with comparable structural properties. We also discuss the thermo-structural behavior of the new MOF materials induced by de- and rehydration, which led to color changes. The materials presented in this work were further characterized using various solid-state techniques. Due to the open metal sites after thermal and hydration activation, the hydrous phase **3** displayed a very good catalytic performance in the oxidation of styrene derivatives using 30% (wt) aqueous H_2O_2 as the oxidant. Moreover, we present a tentative reaction mechanism to illustrate the high catalytic activity and selectivity for the catalytic oxidation using **3**.

2. EXPERIMENTAL SECTION

2.1. Materials and Physical Measurements. Solvents were dried and distilled prior use. The hydrated copper(II) salts ($Cu(OAc)_2\cdot 2H_2O$ and $CuCl_2\cdot 2H_2O$), 1,2,4,5-benzenetetracarboxylic acid (H_4btec), deuterated solvents (D_2O and $CDCl_3$), and other reagent-grade chemicals were purchased from commercial suppliers (Sigma-Aldrich, Germany or South Africa) and used as received. The bulk sample of H_4btec was purified by recrystallization before it was used. All solvents were purchased from either Protea Chemicals (South Africa) or BM Scientific/Parow Industrial (South Africa) and Ranbaxy Fine Chemicals Ltd. (India).

Elemental microanalysis was carried out on an Elementar Analysensysteme varioMICRO V1.6.2 GmbH analysis system. Atomic absorption spectroscopy (AAS) results were obtained using a Varian 1275 spectrometer with a laminar acetylene burner. All infrared (IR) spectra were acquired using a PerkinElmer Spectrum 100 spectrometer with a KBr beam splitter and an attenuated total reflection (ATR) attachment. Mid-infrared spectra ranging from 4000 to 650 cm^{-1} (note: br—broad, m—medium, sh—shoulder, s—strong, vs—very strong, and w—weak) were obtained by positioning the samples on a diamond/ZnSe crystal plate and employing a force gauge within the range of 100 to 149.

Ultraviolet−visible (UV−vis) spectra were recorded on a PerkinElmer UV−vis spectrophotometer model LAMBA 25. Proton nuclear magnetic resonance (^{1}H NMR) spectral data were collected using a Bruker Avance III HD 400 MHz NMR spectrometer with tetramethylsilane (TMS) as an internal reference. The coupling constant (*J*) is quoted in Hertz (Hz). Spectra were recorded in deuterated solvents: All chemical shift values are expressed in parts per million (ppm) relative to $CDCl_3$ (δH 7.26) and DMSO-d_6 (δH 2.50).

Samples were analyzed by differential scanning calorimetry (DSC) using a TA DSC 2500 instrument with hermetically sealed TZero aluminum pans and at a heating rate of 10 K·min^{-1}. Hot-stage microscopic analysis was performed using a Linkam THMS 600 microscope stage and a Linkam TMS 93 temperature controller. Thermogravimetric (TG) measurements were carried out on a PerkinElmer TG-4000 (Pyris Version 4.01 software) at a heating rate of 5 K·min^{-1} and with nitrogen gas purge at a rate of 20 mL·min^{-1}. Powder X-ray diffraction (PXRD) patterns were recorded on a Bruker D8 ADVANCE diffractometer with monochromatic Cu Kα radiation. The samples were gently ground at room temperature (RT; 298 K) before being subjected to 2θ range = 5−60° with a scan rate of 1°.min^{-1}. Brunauer, Emmett, and Teller

https://doi.org/10.1021/acsomega.3c05999
ACS Omega 2024, 9, 7511−7528

(BET) surface area measurements were carried out on Micromeritics ASAP 2020 HD analyzer (Accelerated Surface Area and Porosimetry System), determined by nitrogen gas (N_2) adsorption−desorption at 77 K. Samples to be analyzed were degassed with helium gas at 393 K on Flow Prep 060. Essentially, *ca.* 60−85 mg of the activated samples were utilized for the gas adsorption−desorption measurements. Finally, the instrument was used with nitrogen as the analytical gas, and the determination was based on a 5-point method with 30 adsorption and 30 desorption points measured. A custom-built relative humidity (RH) vapor balance was used to report the adsorption and desorption water-vapor isotherms of the dehydrated MOF samples. The RH range employed was between 2 and 70% with an error of 3%. Gas chromatographic-mass spectrometry/gas chromatography (GC-MS/GC) measurements were carried out using an Agilent 7000 Series Triple Quad with an FID detector and a capillary column (Rxi-5Sil MS, column length: 30 m; internal diameter: 0.25 mm).

2.2. Recrystallization/Synthesis of H_4btec and $[Cu_2(btec)(OH_2)_4]\cdot 2H_2O$. *2.2.1. Recrystallization of H_4btec.* The ligand H_4btec was recrystallized from a methanol/water ($MeOH/H_2O$; 70:30%, v/v) mixture at 373 K for 20 min. X-ray crystallography confirmed the molecular structure of the ligand (CCDC 2206312) shown in Figure S1, and crystal data and refinement details are given in Table S1. It is worth noting that the molecular structure of H_4btec has been reported elsewhere.[33]

2.2.2. Synthesis of {$[Cu_2(btec)(OH_2)_4]\cdot 2H_2O$} (1). A solution of $Cu(OAc)_2\cdot 2H_2O$ (22 mg, 0.10 mmol) and H_4btec (12.7 mg, 0.05 mmol) in 3.0 mL of deionized water (d-H_2O) was placed in a Teflon-lined stainless steel vessel. It was heated to 493 K under autogenous pressure for 2 days (as illustrated in Scheme S1) and then cooled to RT. The dark blue block-shaped crystals of **1** were filtered, washed with cold MeOH and then with d-H_2O, and finally air-dried. Yield: 14.1 mg (65%), based on the ligand H_4btec. Selected IR (ATR; cm^{-1}) for **1**: 3424 (vs, br) ν(O−H_{water}); 3243(w) ν(C−$H_{aliphatic}$); 1669 (sh); 1555 (vs) $\nu_{asym}(COO^-)$; 1428 (vs); 1395 (vs) $\nu_{sym}(COO^-)$; 1278 (w); 1136 (w); 933 (m); 901 (m); 866 (s); 815 (s); 761 (m); 693 (m). Anal. Calcd for $C_{10}H_{14}Cu_2O_{14}$ (485.30 g·mol^{-1}): C, 24.75; H, 2.77; Cu, 26.2%. Found: C, 24.84; H, 2.86; Cu, 25.6%.

Subsequently, network **1** was used as a precursor for a two-step SCSC dehydration, accompanied by color changes, to form **2′** and **2″** (Scheme 1; see Results section for a discussion). IR (ATR; cm^{-1}) for **2′**: 3000−2900 (w) ν(C−$H_{aliphatic}$); 1659 (sh); 1559 (vs) $\nu_{asym}(COO^-)$; 1435 (vs); 1401 (vs) $\nu_{sym}(COO^-)$; 920 (w); 909 (w); 869 (m); 825 (s); 802 (s); 760 (s); 676 (s). Anal. Calcd for $C_{10}H_2Cu_2O_8$ (377.21 g·mol^{-1}): C, 31.84; H, 0.53; Cu, 33.7%. Found: C, 31.79; H, 0.48; Cu, 34.2%. IR (ATR; cm^{-1}) for **2″**: 3000−2900 (w) ν(C−$H_{aliphatic}$); 1699 (sh); 1559 (sh); 1544 (m) $\nu_{asym}(COO^-)$; 1485 (s); 1365 (s); 1305 (m) $\nu_{sym}(COO^-)$; 1135 (m); 944 (m); 870 (m); 840 (w); 815 (s); 766 (s); 731 (sh); 697 (sh). Anal. Calcd for $C_{10}H_2Cu_2O_8$ (377.21 g·mol^{-1}): C, 31.84; H, 0.53; Cu, 33.7%. Found: C, 31.77; H, 0.49; Cu, 34.1%.

In another experiment, **2′** was employed for the synthesis of **3** *via* room-temperature semireversible water-induced SCSC transformation. IR (ATR; cm^{-1}) for **3**: 3667−2992 (vs, br) ν(O−H_{water}); 3000−2900 (w) ν(C−$H_{aliphatic}$); 1663 (s); 1572 (s); 1546 (vs) $\nu_{asym}(COO^-)$; 1503 (w); 1392 (vs) $\nu_{sym}(COO^-)$; 1136 (m); 942 (sh); 926 (w); 868 (m); 823 (s, br); 788 (sh); 762 (w); 673 (w). Anal. Calcd for $C_{10}H_6Cu_2O_{10}$ (413.24 g·mol^{-1}): C, 29.06; H, 1.34; Cu, 30.8%. Found: C, 28.97; H, 1.39; Cu, 31.2%. Thermal dehydration (at ≥393 K) of **3** induced irreversible crystal degradation and the formation of an amorphous phase. The syntheses of **2′_r** and **2″_r** were achieved *via* room-temperature reversible water-induced SCSC transformation of **2′** and **2″**, respectively. Notably, these water-triggered SCSC transitions of **2′** and **2″** (monitored every 24 h over 10 weeks) were replicated at least three times and produced only frameworks **3**, **2′_r**, and **2″_r**. Additionally, despite their low crystallinity (after numerous attempts, improving the quality of the crystals proved futile), **2′_r** and **2″_r** were unambiguously confirmed by single-crystal X-ray diffraction. Crystal structures of **2′_r** and **2″_r** (CCDC 2274951−2274952) are shown in Figure S2, while their crystallographic and refinement data are summarized in Table S1.

Scheme 1. Optical Microphotographic Images for Single Crystals of 2′ and 2″ from SCSC Dehydration of Pristine Framework 1, as well as 3 from Semireversible SCSC Dehydration of As-Obtained Framework 2″

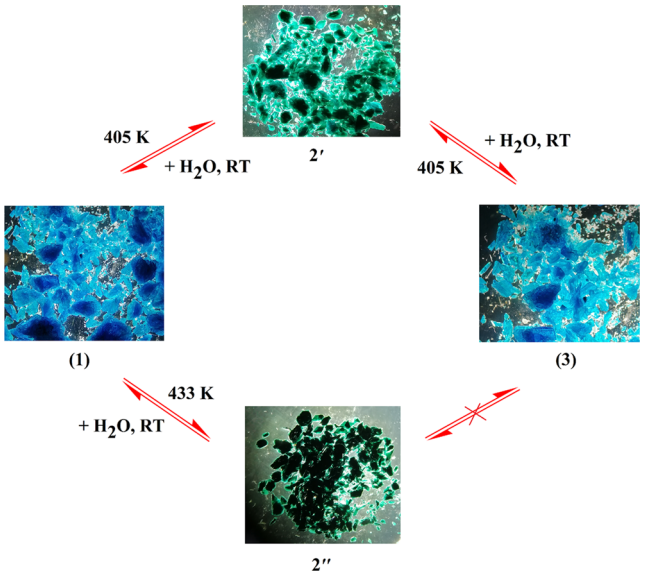

2.3. X-ray Crystallography. Single crystals of the coordination frameworks were selected individually under a polarized light microscope, glued to the end of glass fibers and mounted on goniometer heads under a liquid nitrogen stream.

Full-intensity solution data sets were collected at 150 K on a Bruker D8 VENTURE with a Photon III detector diffractometer[34,35] equipped with a graphite monochromator and Mo Kα (λ = 0.71073 Å), with a fine-focus sealed tube operated at 2.0 kW (50 kV, 40 mA). All reflections were emerged and integrated with Bruker SAINT and XPREP software packages, respectively.[36] Data were collected for absorption effects using the multiscan techniques SADABS,[37] and the structures were solved by the direct methods package SHELXT and refined using X-Seed software incorporating SHELXL.[38,39] The final anisotropic full-matrix least-squares refinement was done on F^2. The aromatic protons were placed in geometrically idealized positions (C−H = 0.93−0.95 Å) and constrained to ride on their parent atoms with $U_{iso}(H) = 1.2U_{eqv}(C)$. SHELX constraints and restraints were used to model the structures. The non-hydrogen atoms were refined with anisotropic displacement parameters. The crystallographic

https://doi.org/10.1021/acsomega.3c05999
ACS Omega 2024, 9, 7511−7528

Table 1. Crystallographic Data and Refinement Details of 1−3

compounds	1	2′	2″	3
empirical formula	$C_5H_7O_7Cu$	C_5HO_4Cu	C_5HO_4Cu	$C_5H_3O_5Cu$
F. W. (g·mol^{-1})	242.66	188.61	188.61	206.62
T (K)	150.0(2)	150.0(2)	150.0(2)	150.0(2)
wavelength (Å)	0.71073	0.71073	0.71073	0.71073
crystal habit	block	block	block	block
crystal color	dark blue	light green	dark green	blue
system, space group	triclinic, P-1	monoclinic, $C2/m$	monoclinic, $C2/m$	triclinic, P-1
a (Å)	6.4928(4)	6.5563(11)	6.5701(14)	5.5958(5)
b (Å)	6.8632(4)	17.265(3)	17.271(4)	5.9631(6)
c (Å)	9.3302(5)	4.6542(8)	4.7022(10)	9.3686(9)
α (deg)	95.598(2)	90.00	90.00	89.727(3)
β (deg)	108.838(2)	121.406(5)	122.183(7)	73.270(3)
γ (deg)	107.976(2)	90.00	90.00	81.244(4)
vol. (Å^3)	365.20(4)	449.65(13)	451.59(18)	295.64(5)
Z, Z'	2, 1	4, 1/2	4, 1/2	2, 1
$D_{calcd.}$ (g·cm^{-3})	2.207	2.786	2.774	2.321
μ (mm^{-1})	2.995	4.775	4.775	3.654
F(000)	244.0	368.0	368.0	204.0
crystal size (mm^3)	0.226 × 0.218 × 0.189	0.226 × 0.218 × 0.189	0.226 × 0.218 × 0.189	0.226 × 0.218 × 0.189
hkl ranges	$-8\leq h\leq 8$	$-8\leq h\leq 8$	$-8\leq h\leq 8$	$-6\leq h\leq 6$
	$-9\leq k\leq 9$	$-21\leq k\leq 21$	$-21\leq k\leq 21$	$-7\leq k\leq 7$
	$-12\leq l\leq 12$	$-5\leq l\leq 5$	$-5\leq l\leq 5$	$-11\leq l\leq 11$
2θ range (deg)	4.728−56.784	9.172−47.36	7.700−52.74	4.544−52.80
no. reflns.	39,874	5241	11,604	22,756
unique reflns.	1825	476	477	1208
completeness to θ (%) on F^2	100.0	100.0	100.0	99.0
absorption correction	multiscan	multiscan	multiscan	multiscan
data/restrains/parameter	1825/0/124	476/0/47	477/0/48	1208/0/102
R(int)/R(sigma)	0.0351/0.0167	0.0527/0.0243	0.0724/0.0200	0.0500/0.0164
GOF	1.072	1.156	1.174	1.128
R_1/wR_2 [I > 2σ(I)][a]	0.0190/0.0492	0.0536/0.1315	0.0808/0.1963	0.0597/0.1354
R_1/wR_2 (all data)[b]	0.0195/0.0498	0.0586/0.1359	0.0899/0.2042	0.0784/0.1543
max./min e$^-$ density (e·Å^{-3})	0.74/−0.85	1.13/−0.93	2.42/−1.20	1.13/−0.81
CCDC number	2206282	2206283	2206284	2239239

[a] $R_1 = \sum||F_o| - |F_c||/\sum|F_o|$. [b] $wR_2 = \{\sum[w(F_o^2 - F_c^2)^2]/\sum[w - (F_o^2)^2]\}^{1/2}$, $w = 1/[\sigma^2(F_o)^2 + (aP)^2 + bP]$, where $P = [F_o^2 + 2F_c^2]/3$.

and refinement data are provided in Table 1. The single-crystal data and diffraction-crystal modules of the Mercury 2020.2.0 program,[40] which are freely available *via* the Internet at https://www.ccdc.cam.ac.uk/, were employed to simulate the PXRD patterns of MOFs.

2.4. Procedure for the Oxidation of Substrates. Prior to each experiment, the catalyst was carefully ground to a fine powder of approximately 0.037 mm using a mortar and pestle. The substrates (10.0 mmol), catalyst (25 mg, approximately 0.01 mol %), and acetonitrile (MeCN; 15.0 mL) were added sequentially to a two-necked round-bottom 25.0 mL flask equipped with a reflux condenser and a small magnetic stirrer bar at RT. The mixture was heated in air (open atmosphere) to 80 °C, and 30% (wt) H_2O_2 (25.0 mmol) was added dropwise with stirring at 300 rpm for 4−6 h. GC-MS was used to quantitatively identify the products. After each successive cycle, the filtered MOF catalysts were collected, rinsed at least three times with d-H_2O, acetone and MeOH, and dried *in vacuo* at 100 °C for 60 min. Before each catalytic cycle, the solvent content was determined using TG analysis, and PXRD experiments were performed to ensure that crystallinity was maintained. Control experiments were conducted to evaluate the role of (a) catalyst loading, (b) reaction time, (c) reaction temperature, (d) molar ratio of styrene to H_2O_2, and (e) solvent.

2.5. Hot Filtration Test. For a hot filtration test, the activated catalyst was removed from the hot reaction mixture by filtration after 1 h, while the reaction was still running for the next 3 h.

3. RESULTS AND DISCUSSION

3.1. Single-Crystal Structure of 1. Complex **1** with the chemical formula $[\mathbf{Cu_2(btec)(OH_2)_4}]\cdot\mathbf{2H_2O}$ crystallizes in the triclinic P-1 (no. 2) space group (Table 1). Notably, the crystal structure of **1** is known and has been previously described.[41] A crystallographically independent Cu(II) center (Cu1), a half $(btec)^{4-}$ anionic ligand, two coordinated H_2O molecules, and one guest H_2O constitute the asymmetric structural unit of **1** (Figure 1a). The step-like 2D structure of **1** is assembled by a secondary building unit (SBU) of Cu-btec composed of a tetradeprotonated ligand coordinated in a triangular fashion with two Cu^{II} ions. The Cu(II) ion is in a general position, while the $(btec)^{4-}$ anion is located on a crystallographic inversion center and thus exhibits C_i symmetry. Each of two p-carboxylate groups of the ligand assume a bidentate bridging coordination mode, while each of the other two adopts a

https://doi.org/10.1021/acsomega.3c05999
ACS Omega 2024, 9, 7511−7528

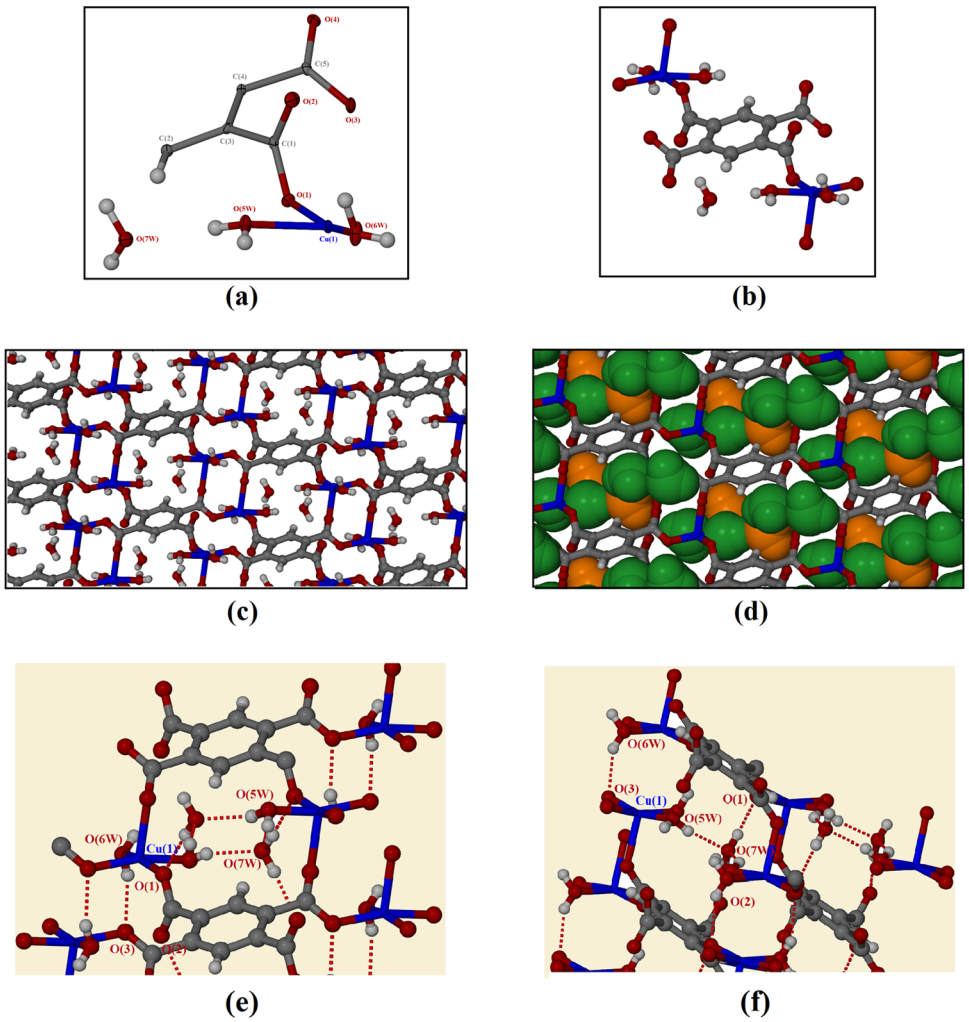

Figure 1. (a) ORTEP diagram for the asymmetric structural unit with partial atom numbering scheme for **1** down the *b*-axis. (b) Ball-and-stick diagram of **1** showing the coordination environment around the Cu(II) atoms. Packing views of a 2D closed framework (both along the *a*-axis): (c) Ball-and-stick diagram showing packing features of **1**. (d) Ball-and-stick with space-filled diagrams for guest (orange) and coordinated (green) H_2O molecules. (e, f) Intermolecular hydrogen bonding interactions along the *a*- and *c*-axes, respectively (color code: Cu, blue; C, gray; O, red; H, off-white).

monodentate coordination mode, and the entire linker acts as a μ_6-bridge connecting six Cu^{II} ions (Figure 1b).

The two carboxylate groups of the $(btec)^{4-}$ ligands bridge two adjacent Cu1 atoms to form a Cu_2 unit with a Cu···Cu distance of 4.191(4) Å in two different coordination modes: μ_1–η^1:η^0 (Scheme 2-I) and μ_2–η^1:η^1 (Scheme 2-III), forming a binuclear $[Cu_2O(COO)_2(OH_2)_4]$ core, which can be considered as the SBU of the structure. The SBP of the Cu^{II} atom (with τ_5 = 0.03; where τ_5 is an Addison parameter[42] suggesting either a SBP (τ_5 = 0 for ideal) or TBP (τ_5 = 1 for ideal) geometry) is completed by two carboxyl oxygen atoms (Cu1–O1 and Cu1–$O3^{i}$ bond lengths are 1.960(13) and 1.959(11) Å, symmetry code: (i) 1 − *x*, 1 − *y*, 2 − *z*), in a *trans* arrangement, by two $(btec)^{4-}$ ligands and two oxygen atoms (Cu–O5W and Cu–O6W bond distances are 1.965(11) and 1.987(14) Å; Tables 2 and S2) in the basal plane and one carboxyl oxygen atom (Cu1–$O4^{ii}$ bond length 2.216(11) Å; symmetry code: (ii) −1 + *x*, −1 + *y*, *z*) from the third carboxyl oxygen atom in the apical position. These bond lengths are comparable with those of frameworks **2′_r** and **2′′_r** (see Tables 2 and S2–S3). Moreover, these bond lengths are comparable to those reported in the literature for analogous Cu(II)-based frameworks.[38] The dihedral angles between the carboxylate groups and the aromatic ring are two of 30.05° and two of 66.75°, respectively, with the monodentate coordinating groups twisted away from the ring plane. The monodentate and bidentate coordination modes of the $(btec)^{4-}$ anion, in addition to the SBP and *trans* coordination mode around each Cu^{II} center, lead to the formation of a planar 2D covalent network that has rectangular channels with dimensions of approximately 6.5 Å × 4.5 Å as viewed along the *ab* plane.

In **1**, the ∠(O–Cu–O) bond angles range from 81.63(5) to 166.41(5)° (Table S4). Additionally, a 3D network (Figure

Scheme 2. Coordination Modes of $(btec)^{4-}$ Observed in 1–3

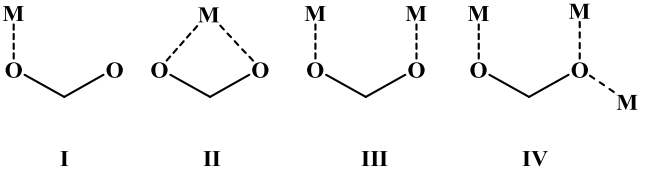

https://doi.org/10.1021/acsomega.3c05999
ACS Omega 2024, 9, 7511−7528

Table 2. Selected Bond Distances (Å) Observed for Frameworks Reported in This Work

	bond distance (Å)					
MOF	Cu···Cu	Cu1−O1[a]/O2[a]	Cu1−O3	Cu1−O4	Cu1−O5W[a]	Cu1−O6W
1	4.191(4)	1.960(13)	1.959(11)	2.216(11)	1.965(11)	1.987(14)
2′	3.476(8)	1.946(4)	n/a	n/a	n/a	n/a
		1.946(4)				
		2.500(6)				
2″	3.482(11)	1.940(7)	n/a	n/a	n/a	n/a
		1.940(7)				
		2.532(9)				
2′_r	4.194(2)	1.942(6)	1.958(8)	2.218(6)	1.969(8)	1.971(7)
2″_r	4.202(3)	1.946(10)	1.971(10)	2.222(9)	1.971(11)	1.947(9)
3	2.764(14)	1.953(5)	1.955(5)	1.954(5)	1.944(6)	n/a
					2.507(5)	

[a]Mixed bridging and nonbridging oxygen atom; n/a stands for "not applicable".

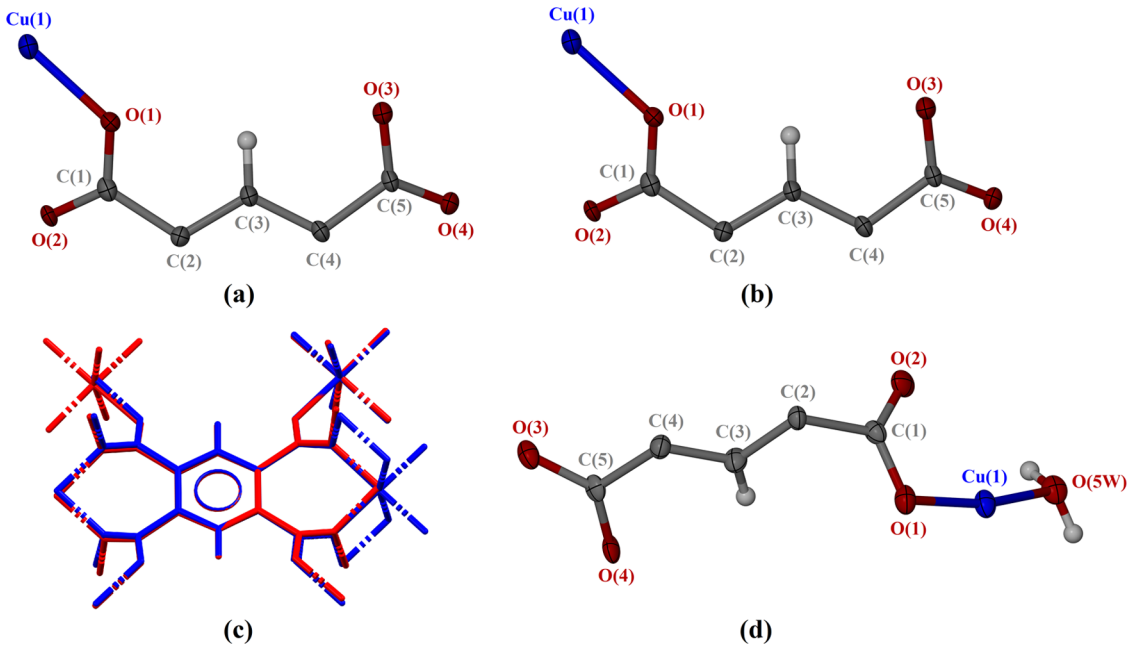

Figure 2. (a) Asymmetric unit of **2′** viewed along the *a*-axis (color code: Cu, blue; C, gray; O, red; H, off-white). (b) Asymmetric unit of **2″** viewed down the *a*-axis. (c) Overlay of **2′** (blue) and **2″** (red) as displayed by Mercury. (d) Asymmetric unit of **3** viewed along the *bc* plane.

1c,d) is generated *via* connections between covalently bonded polymeric structures consisting of direct O−H···O interactions (Figure 1e,f and Table S5) facilitated by coordinated and guest H_2O molecules.

3.2. First and Second SCSC Transformations: 1 → 2′ and 1 → 2″. Upon drying the crystals *in vacuo* at 403 and 433 K for 6 h, **1** undergoes phase transitions to produce **2′** (light green) and **2″** (dark green) both with crystal formula [**Cu_2(btec)**]. Numerous efforts to prepare **2′** and **2″** by direct routes (*i.e.* **2′** → **2″** or **2″** → **2′** through heating/cooling, etc.) or by obtaining **1** from **2′**/**2″** *via* exposure to H_2O vapor were attempted to no avail. However, a phase transition was observed during the structural transformation to produce **2′** and **2″** and their lattice parameters undergo a significant variation, representing approximately 39.0% volumetric shrinkage (on the basis of the initial volume of **1**). Furthermore, **2′** and **2″** have the identical monoclinic *C*2/*m* (no. 12) space group (both collected at 150 K), but their unit cell parameters differ somewhat.

These 3D architectures are composed of dimeric cationic Cu(II) units and bridging $(btec)^{4-}$ anions, displaying the same connectivity and chemical formula. The crystal structure of these materials comprises an asymmetric unit with one-half of Cu(II) cation and one-quarter of the $(btec)^{4-}$ bridging ligand (Figure 2a,b). The coordination environment around the metal center of each structure is a hexacoordinate distorted O_h geometry $\{CuO_6\}$ with four oxygen atoms of carboxylate groups belonging to two different ligands coordinating in a μ_3−η^1:η^2 (Scheme 2-IV) manner. Moreover, the central Cu(II) ion of **2′** has essentially the same coordination environment as **2″** and this is neatly exemplified by their overlay (Figure 2c). The calculated RMSD value of the two isolated frameworks ({Cu1, O1, C1···} to {Cu1, O1, C···} without inversion) is 0.790 Å. Both forms show an overall similar structural topology with only slight changes in their bond distances (Table 2) and angles.

All of the water molecules in both **2′** and **2″**, guest and coordinated, have been evacuated and the networks are now composed of four crystallographically unique Cu(II) centers

https://doi.org/10.1021/acsomega.3c05999
ACS Omega 2024, 9, 7511−7528

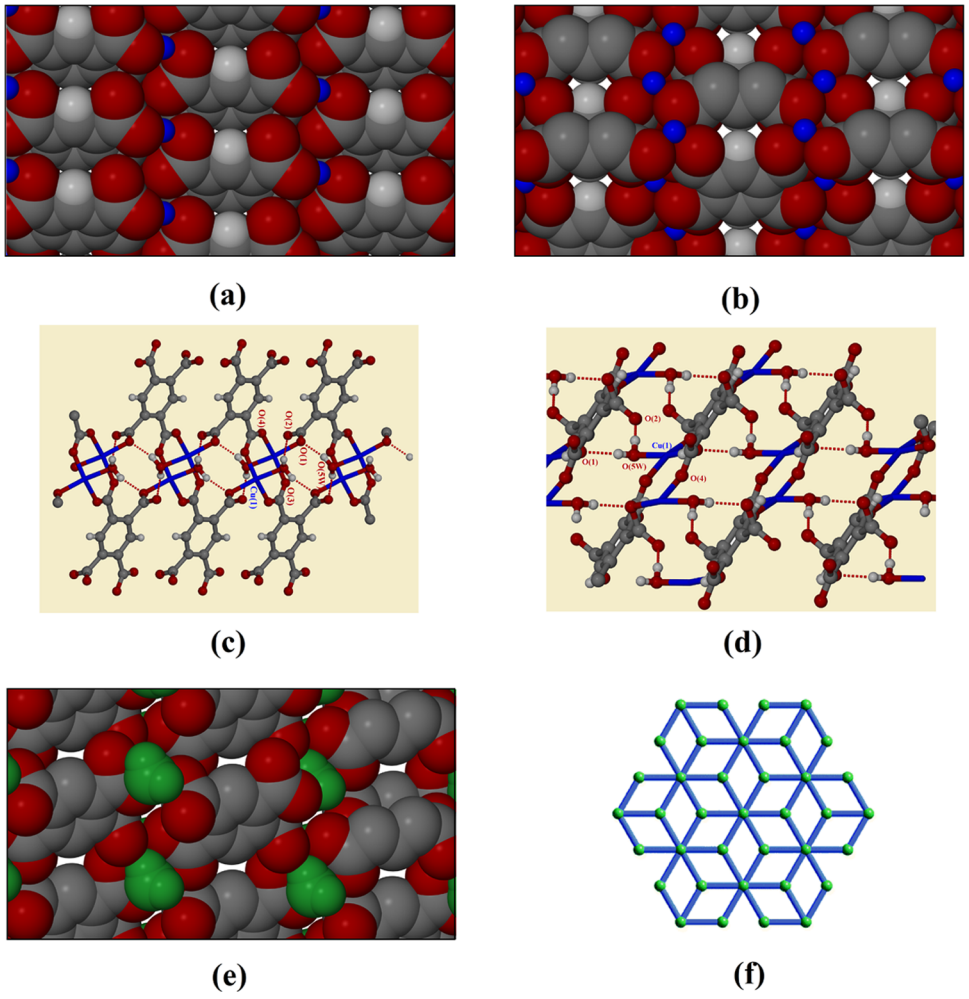

Figure 3. Space-filled diagrams for (a) **2′** and (b) **2″** (both along the *b*-axis). (c, d) Intermolecular hydrogen bonding interactions down the *b*- and *c*-axes, respectively. (e) Space-filled diagram for **3** (along the *c*-axis) together with coordinated (green) water molecules: color code: Cu, blue; C, gray; O, red; H, off-white. (f) Topological representation of the (3,6)-connected **kgd** net realized along the arbitrary axis.

(arranged into distinct $\{Cu_2(COO)_4\}$ paddle-wheel units)[41,43] and four unique $(btec)^{4-}$ SBUs. These anhydrous lattices exhibit structurally similar hexagonal grids with *ca.* 7.0 Å × 5.0 Å (down *b*-axis) dimensions. Additionally, these dehydrated materials have deformed such that on half of the Cu(II) paddle-wheel SBUs, the coordination sites that were vacated by the apical coordinated water molecules are now occupied by two carboxylate oxygen atoms. Therefore, this alters the coordination sphere of the metal centers in the paddle-wheel architectures, which causes the variation of dimensionality from the 2D layer in **1** to 3D frameworks in both **2′** and **2″**.

Furthermore, the remaining half of the paddle-wheel units are assembled such that the two pairs of the Cu−O bond lengths in **2′** and **2″** are identical, reflected in different torsion angles (∠(O2−Cu1−O1−C1), 131.1(6)° and 132.6(10)°, respectively). Due to Jahn−Teller distortion of the dimeric Cu(II) centers, Cu−O bonds are axially elongated in both structures. Accordingly, the Cu1−O1^{i} bond lengths are 1.946(4) and 1.949(4) Å in **2′** and 1.940(7) and 1.950(8) Å in **2″** (Tables 2 and S6−S7); with symmetry code: (i) $1 - x, y, 2 - z$. In **2′** and **2″**, the intermetallic distances are 3.476(8) and 3.482(11) Å, respectively. The shortest paddle-wheel Cu···Cu distance in the literature is commonly about 2.601(4) Å,[44] and the longest is 4.730(1) Å.[45] Therefore, these bond lengths are within normal statistical errors. In addition, the (∠O−Cu−O) bond angles vary from 77.99(19) to 168.06(12)° in **2′** and from 78.80(3) to 167.9(2)° in **2″** (Tables S6−S7). We may note that frameworks **2′** and **2″** have no classical hydrogen bonds (Table S5). Furthermore, SCSC phase transitions further affected the $\pi-\pi$ interactions to form almost nonporous networks (Figure 3a,b). After the two-step transformations, phenyl rings were determinately separated and the distance between them is 4.654(5) and 5.731(5) Å for **2′** (directed along the *a*- and *b*-axes), with **2″** displaying comparably wider and narrower centroid distances of 4.702(8) and 5.689(8) Å (oriented along the *c*- and *a*-axes), respectively (Figure S4a,b). Moreover, in **2′** and **2″**, the angle between the planes of the respective phenyl rings is 0.00°.

3.3. Third SCSC Structural Transformation. Interestingly, when the small crystals of **2′** were immersed in 2 mL of d-H_2O at RT for 3 days (no changes were observed after the first and second days), a monohydrated complex with chemical formula $[\mathbf{Cu_2(btec)(OH_2)}]$ (**3**) was formed. Single-crystal X-ray diffraction analysis revealed that **3** crystallizes in *P*-1 (no. 2) space group.

In essence, the water-induced semireversible transformation from anhydrous **2′** to hydrous **3** results in a slight increase of the unit cell, with the space group change from the monoclinic

https://doi.org/10.1021/acsomega.3c05999
ACS Omega 2024, 9, 7511−7528

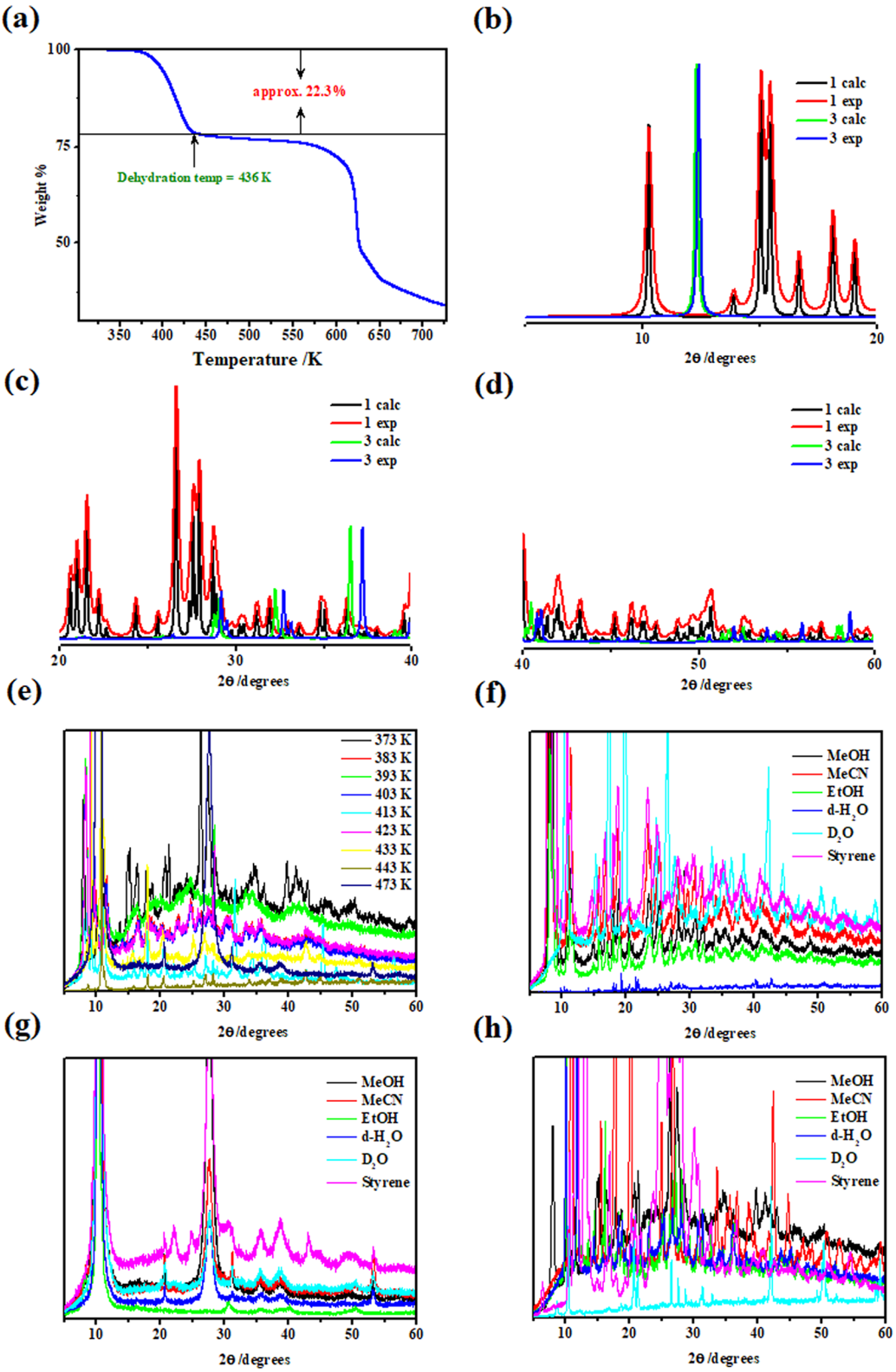

Figure 4. Crystal transformation monitored by TG and PXRD measurements. (a) TG curve of **1** with a heating rate of 5 K.min^{-1}. The total weight loss of approximately 22.3 ± 0.05% at *ca.* 303−436 K suggests that three H_2O molecules are eliminated in the two-step transformation upon heating. (b−d) Comparative diffractions from top to bottom: truncated PXRD patterns (calculated and experimental) of hydrous frameworks **1** and **3**. (e) Variable-temperature PXRD of **1**. The diffraction phases correspond to **2′** (observed at 403−423 K) and **2″** (at 433−473 K). Representative PXRD diffractograms for several classes of solvent immersion (from the bottom: MeOH, MeCN, EtOH, d-H_2O, deuterated water (D_2O)) and styrene; (f) **2′**, (g) **2″**, and (h) **3**.

(high symmetry) to the triclinic (low symmetry) crystal system. The asymmetric structural unit constitutes one crystallographically independent Cu(II) center (Cu1) and half $(btec)^{4-}$ anionic ligand, without any guest molecules

https://doi.org/10.1021/acsomega.3c05999
ACS Omega 2024, 9, 7511−7528

present (Figure 2d). In **3**, the Cu1 center adopts a slightly distorted SBP configuration, which is defined by three oxygen donors from two different $(btec)^{4-}$ ligands and one oxygen atom derived from the coordinated bridging H_2O (μ_2-OH_2) molecule. The μ_3–η^1:η^2 (Scheme 2-IV) bridging mode of the carboxylates in **2′** changes to μ_1–η^1:η^1 (Scheme 2-II) and μ_2–η^1:η^1 (Scheme 2-III) in **3**. The Cu···Cu interatomic distance in the $\{Cu_2(COO)_4(OH_2)_2\}$ core is significantly reduced from 3.476(8) to 2.764(14) Å, resulting in a remarkable rearrangement of this structural motif. In comparison to **2′**, the Cu1 atom of **3** has a distorted SBP geometry (τ_5 = 0.072;), with all of the basal Cu1–O (O1, $O3^{i}$, $O4^{ii}$, and $O5W^{iii}$) bond lengths extending somewhat more than 0.028 (symmetry codes: (i) $x, y, -1 + z$; (ii) $1 - x, 2 - y, 1 - z$; (iii) $1 - x, 2 - y, -z$). Interestingly, one oxygen atom (μ_2-O5W) forms an unusual bridge between two Cu(II) centers with bond distances 1.944(5) and 2.507(5) Å (Tables 2 and S8), creating a pentacoordinate geometry. The distance between two Cu(II) spheres bridged by H_2O as a ligand is reported to be between 2.841 and 3.768 Å.[46−48] The lengths of $Cu–O_{carboxylate}$ bonds range from 1.951(5) to 2.546(5) Å, which is within the normal range.[49,50] It is noticeable that the bond length of $Cu–O_{basal}$ elongated (typical Jahn–Teller distortion) while that of $Cu–O_{apical}$ shortened when the aqua molecule bridged the two Cu(II) centers in **3**. As shown in Table S8, the *cis* and *trans* (∠O–Cu–O) angles are in the range of 56.5(2)–104.4(2)° and 164.6(2)–168.9(2)°, respectively.

The fully deprotonated $(btec)^{4-}$ acts as a bidentate ligand coordinated with two binuclear Cu^{II} units to form a rectangular window with approximately 8.0 Å × 5.0 Å (down *c*-axis) dimensions. The adjacent rings are spatially connected to form 1D double chains. Furthermore, intermolecular forces and hydrogen bonding interactions (Figure 3c and Table S5) mediated by water molecules extend the 2D supramolecular layers into a microporous framework (Figure 3d and Table S9).

3.4. Characterization Studies of Precursors 1, 2′, 2″, and 3. PLATON software[51] was employed to examine the number of water molecules and void spaces in **1**–**3**. Network **1** became unstable in the triclinic system due to the huge void space of 103.4 $Å^3$ (28.3% solvent-accessible void) after the guest and coordinated aqua molecules were eliminated, and it was converted to a monoclinic system of both **2′** and **2″**. However, no solvent-accessible void space was found for **2′**, **2″**, and **3**. From topological viewpoint, the as-synthesized MOF, the dehydrated as well as the rehydrated frameworks, all possess a (3,6)-connected Kagomé-dual (**kgd**) topology (Figure 3e) with point (Schläfli) symbol $\{4^3\}_2\{4^6\}$. Furthermore, complexes **1**–**3** were further characterized by IR, thermal analysis (TG, DSC, and HSM), PXRD, and gas and moisture sorption isotherm studies at 77 and 298 K.

3.4.1. Infrared (IR) and Ultraviolet–Visible (UV–vis) Spectra. The IR spectra, together with the list of the most intense bands and their assignations, are shown in Figure S5. The characteristic bands of the $(btec)^{4-}$ ligands are visible in all four spectra, as evidenced by a set of different overlapped frequencies around 1630 cm^{-1} related to asymmetrical and symmetrical stretching of C=O bonds from carboxylate groups. The above frequencies are indicative of a $(btec)^{4-}$ ligand with various coordination modes (*i.e.* monodentate, bidentate, bridging). For all frameworks, a broad band centered at *ca.* 3082 cm^{-1}, which corresponds to the stretching O–H vibrations from water molecules, was observed. Although this O–H band can still be seen in the spectra of the two dehydrated materials, it is suggested that this vibrational band is caused by humidity absorbed by the KBr matrix and does not necessarily indicate the presence of coordinated and guest water molecules.

Furthermore, UV–vis spectra were carried out to acquire a better understanding of the crystal transformations. Essentially, a substantial absorption was realized at 750 nm during the transformation of both **2′** and **2″** into **3** and eventually back to **1**. The maximal absorption was the same for both anhydrous phases (therefore, only the spectra of **2′** are reported), inferring the release of a common segment, most likely $\{Cu_2(btec)\}$. Figure S6 displays a maximum peak intensity between 1 and 6 days, demonstrating that **2′** dissolves faster than **3** and **1** crystallize. Beyond this point, the intensity of the maximum absorption peak decreased, showing that the dissolution speed of **2′** and crystallization rates of both **3** and **1** possessed reverse behavior in the second part of the transformation. Consequently, we surmise that dissolution of **2′** and crystallization of both **3** and **1** occur concurrently, while the metal species and linker exist as Cu segments in aqueous solution during the dissolution–recrystallization process.

3.4.2. Thermal Analysis. In the thermogravimetric (TG) curve of **1** (Figure 4a), the weight loss of approximately 7.52 ± 0.13% (calcd 7.421%) and 14.9 ± 0.07% (calcd 14.85%) at *ca.* 303–438 K accounts for 2 lattice and 4 coordinated aqua molecules, respectively. Meanwhile, TG measurements (Figure S7) show that both anhydrous frameworks retain their structural integrity up to 573 K. Such highly thermally stable MOFs could be used as heterogeneous catalysts in higher-temperature organic transformations. Differential scanning calorimetry (DSC) for **1** reveals two exothermic peaks between 303–373 K (dehydration step) and 373–471 K (one-step phase transition), corresponding to transitions observable on a hot-stage microscope (HSM; Figure S8). In the cooling DSC profile shown in Figure S9, no endothermic peak was observed, thus indicating that the transformation is irreversible under N_2 atmosphere.

Figure S8 shows a visual representation (HSM photographs) of the loss of H_2O vapor as bubbles form in silicone oil when crystals of **1** are heated between 373 and 463 K. At 373–413 K, the crystal color lightens from dark to light blue. By 403 K, the crystal is light green and changes to dark green at 433 K. The color change is a consequence of change in the coordination sphere around the Cu(II) ion (monocoordinated carboxylate becomes bidentate coordination). The difference in the onset temperature (phase transition) between HSM and DSC is most likely due to the different environments in which they are carried out (open *vs* closed).

3.4.3. Powder X-ray Diffraction (PXRD) Studies and Chemical Stability Test. The good match between the experimental powder and single-crystal X-ray diffraction (calculated data) patterns confirms the high crystallinities and good phase purity of **1** and **3** (Figure 4b). To eliminate any ambiguity, temperature-dependent PXRD experiments in the temperature range of 373–473 K were also performed to monitor the phase transition of **1** → **2′** and **1** → **2″**. As shown in Figure 4c, the diffraction peaks representing the structure of **2′** and **2″** emerge as new peaks upon heating the framework to 403 and 433 K, respectively, with the latter phase being retained until crystallinity is lost at *ca.* 473 K. The sharp diffraction peaks indicate that the good-quality crystal lattice is

https://doi.org/10.1021/acsomega.3c05999
ACS Omega 2024, 9, 7511−7528

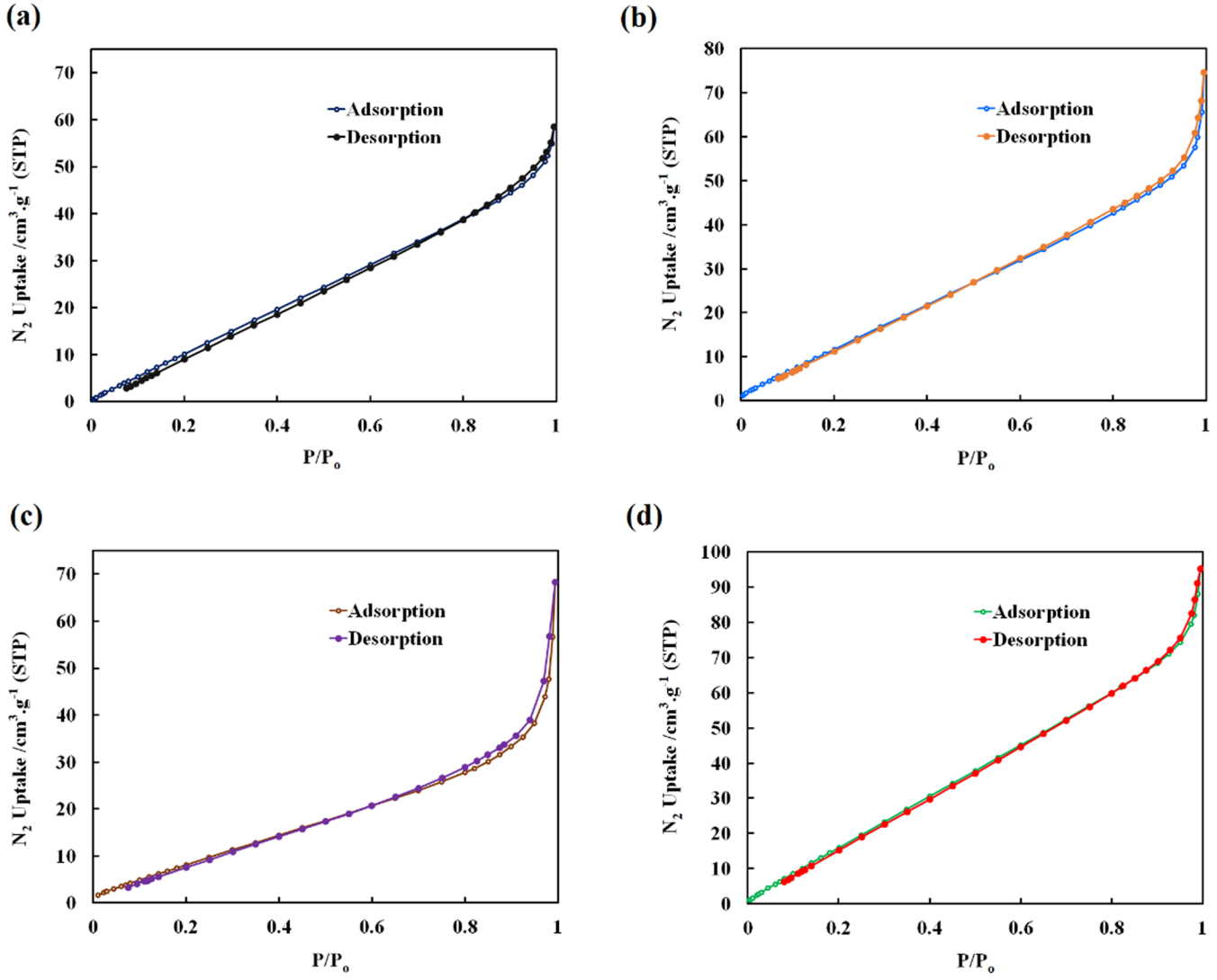

Figure 5. Nitrogen (N_2) sorption isotherms of (a) **1**, (b) **2′**, (c) **2″**, and (d) **3** collected at 77 K (open and closed symbols denote adsorption and desorption, respectively).

preserved after the two-step transformation. However, the transition temperature in the PXRD profile is slightly lower than that in the TG curve, which can be attributed to the different heating methods used in the variable-temperature PXRD and TG measurements. Subsequently, about 50 mg of each material was tested for solvent sustainability in 2.0 mL of MeOH, MeCN, ethanol (EtOH), d-H_2O, deuterated water (D_2O), and styrene at RT for 1−2 weeks. When small-sized crystals of the dehydrated forms were soaked in d-H_2O, the color changed from light green **2′** to blue **3**, but a dark blue color change was only observed after 1 week to yield **1** (herein designated as **2′_r**). Similarly, structural transformation from **2″** to **1** (denoted **2″_r**) was only noticed after 1 week. Both the structures of the restored phases **2′_r** and **2″_r** upon RT rehydration were verified by PXRD and TG measurements (Figures S10−S11a,b). It is therefore concluded that the transformations are genuinely reversible, *i.e.*, **1** ↔ **2′** and **1** ↔ **2″**. X-ray diffraction studies, on the other hand, established that rehydration *via* immersion of either **2′** or **2″** phase and **3** is irreversible when d-H_2O was replaced by D_2O even after 8 weeks. Furthermore, a subsequent color change from green to navy blue was observed when the anhydrous species were subjected to styrene. In contrast, after immersion in MeOH, MeCN, EtOH, and D_2O, the original colors of all three frameworks remained unchanged.

However, PXRD experiments revealed that after 24 h of soaking in aprotic and protic solvents, **2′**, **2″**, and **3** (Figure 4d−f) are well-consistent with those of the dehydrated and semireversible materials, indicating their excellent chemical stability.

3.4.4. Gas and Water Sorption Properties. N_2 adsorption/desorption measurements were carried out for **1**−**3** at 77 K to assess their permanent porosity. As illustrated in Figure 5, typical type III (according to the IUPAC classification) isotherms were achieved for all degassed samples, and the saturated N_2 uptakes were 0.0986, 0.146, 0.148, and 0.176 cm^3 g^{-1} (STP) for **1**, **2′**, **2″**, and **3**, respectively, demonstrating the Brunauer−Emmett−Teller (BET) surface area of approximately 45.29, 86.07, 84.39, and 112.87 m^2 g^{-1}. Based on the N_2 uptake data, the pore size distributions of the four MOF scaffolds were measured, and that of the as-synthesized **1** was mainly around 112.3 Å, with **2′** at 69.9 Å, **2″** at 62.6 Å, and the partially rehydrated **3** at 101.1 Å, agreeing with those estimated from crystal structures (Table 3) and suggested their high

https://doi.org/10.1021/acsomega.3c05999
ACS Omega 2024, 9, 7511−7528

Table 3. Summary of Structure and Porosity Characteristics in 1−3 MOFs

MOF	solvents[a]	cavity size[b] (Å)	void space (%)	BET surface ($m^2 \cdot g^{-1}$)
1	6	5.5 × 3.8	28.3	45.29
2′	0	7.5 × 4.7	–	86.07
2″	0	7.5 × 4.9	–	84.39
3	1	8.0 × 5.0	–	112.87

[a]Guest and/or coordinated H_2O molecules per unit cell. [b]Viewed down the *b*- or *c*-axis.

crystallinity. The vapor sorption isotherm of **2′** displayed a 0.297 $g \cdot g^{-1}$ water uptake from 2 to 70% relative humidity (RH) at RT, with the majority of the adsorption occurring between 20 and 40% RH (Figure S12). At this point, **2′** had reached its maximum capacity. It is worth mentioning that the total amount of water molecules in **1** derived from SC-XRD and TG data (namely, 6.0 molecules per $\{Cu_2(btec)\}$ unit) agrees perfectly with the water-vapor adsorbed amount obtained for **2′** at RT (6.2 molecules per $\{Cu_2(btec)\}$ unit). Essentially, these results confirmed that the dehydrated MOF sample has RT reversible water uptake even at 70% RH.

3.5. Selective Catalytic Oxidation of Substrates. In this case, these findings confirm that temperature-induced structural transformations are advantageous to increasing specific surface area. MOF-based catalysts with larger specific surface areas and pore volumes will expose more catalytic active sites and molecular channels, which is advantageous to the contact between the substrate and active site, as well as the diffusion and transport of the substrate molecule, thereby further increasing their catalytic performances. Networks **1−3**, in general, have clear crystal structures and can serve as ideal heterogeneous catalytic models for the selective oxidation of styrene derivatives. As illustrated in Figure 6a, styrene conversion and product selectivity toward benzaldehyde increase as the amount of **3** increases from 0 to 30 mg, reaching a high conversion of approximately 56% with 99% selectivity at the catalyst dosage of 25 mg (Table S10, entries 1−6). When the catalyst dosage is increased to 30 and 35 mg, the corresponding results slightly decreased (Table S10, entries 6 and 7). As a result, 25 mg (at 0.01 mol % based on $\{Cu_2(COO)_4(OH_2)_2\}$ paddle-wheel) of the catalyst is recommended as the optimal amount. The temperature of the reaction has a significant impact on the reaction rate and pathway. Moreover, catalytic experiments were carried out at 60−90 °C to determine the effect of reaction temperature. Styrene conversions improve considerably as the reaction temperature increases (Figure 6b), from 17% (at 60 °C) to

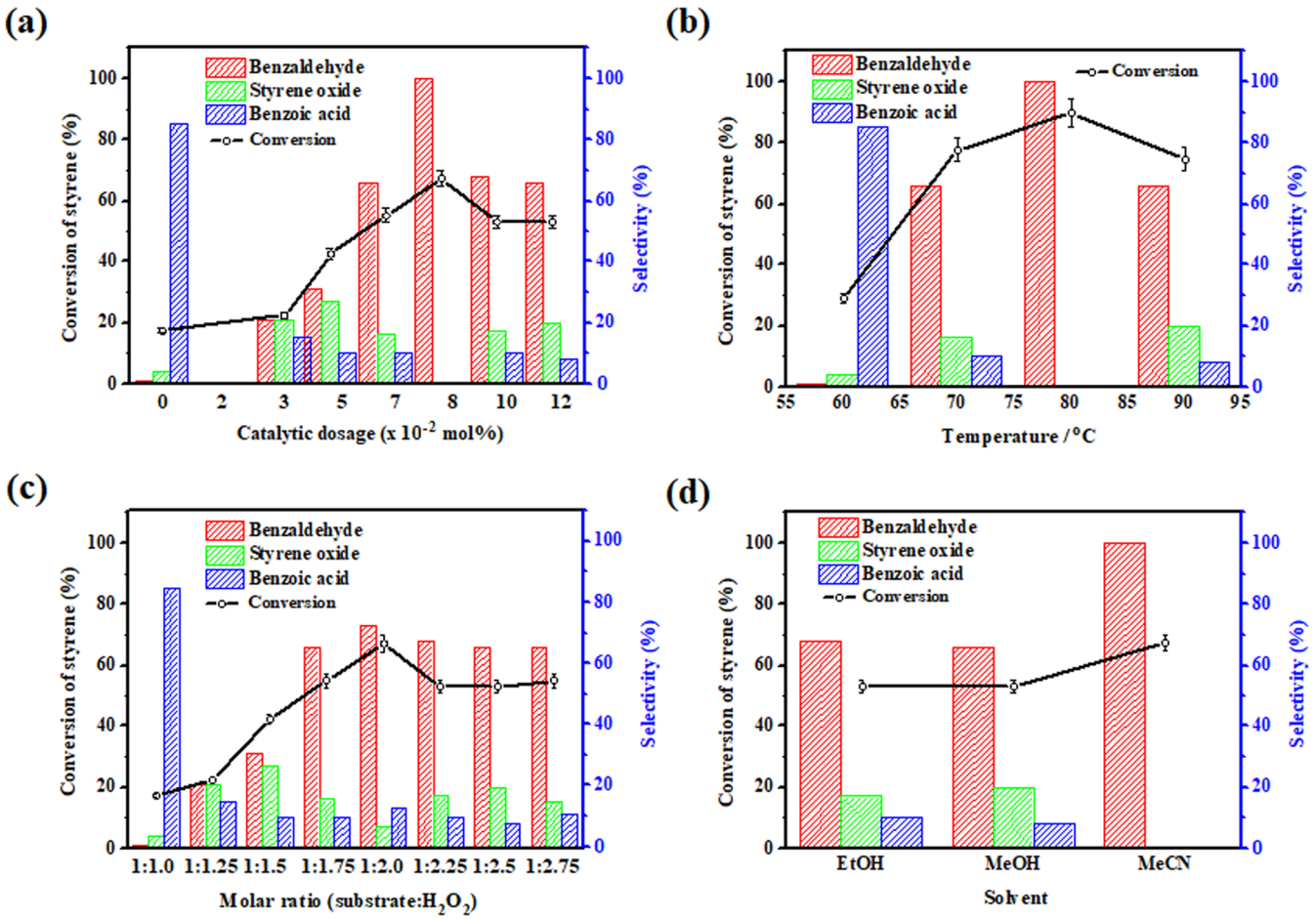

Figure 6. (a) Effect of catalytic dosage of **3** (in mol %) on catalytic performance for selective oxidation of styrene to benzaldehyde. (b) Influence of reaction temperature on the catalytic performance for selective oxidation of styrene to benzaldehyde. (c) Effect of different molar ratios of styrene to H_2O_2 on the catalytic performance for selective oxidation of styrene to benzaldehyde. (d) Influence of different solvents on the catalytic performance for selective oxidation of styrene to benzaldehyde. Reaction conditions: styrene (10.0 mmol) and solvent (15.0 mL) at 80 °C for 4 h. The product yields were determined by GC-MS spectra. The line diagrams and histograms represent the conversion and selectivity, respectively.

https://doi.org/10.1021/acsomega.3c05999
ACS Omega 2024, 9, 7511−7528

Table 4. Catalytic Performances of 1−3 Catalysts in the Oxidation of Styrene to Benzaldehyde[a]

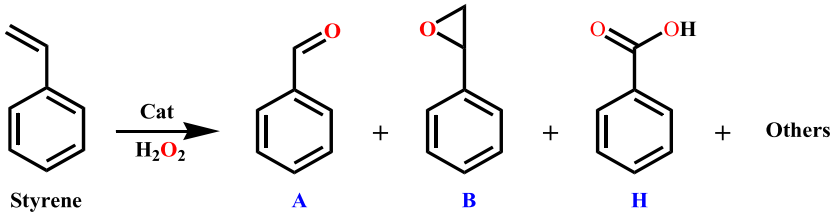

						selectivity[d]		
entry	cat.	time (h)	conv. (%)	TON[b]	TOF[c] (h^{-1})	A	B	H
1	**3**	4	67	82.6	20.7	100	n/a	n/a
2	**2″**	4	59	73.0	18.3	82	8	n/a
3	**2′**	4	54	72.4	18.1	73	9	6
4	**1**	4	40	58.0	14.5	69	2	10

[a]Reaction conditions: styrene (1.15 mL, 10.0 mmol), catalyst (25 mg, *ca.* 0.01 mol %), molar ratio of styrene to H_2O_2 (1:2.5), and MeCN (15.0 mL) at 80 °C. [b]Turnover number (TON) = (moles of product per mole of the dimeric Cu(II) cluster of each catalyst). [c]Turnover frequency (TOF) = TON/time. [d]All values are based on GC-MS spectra. Oxidative products: benzaldehyde (**A**), styrene oxide (**B**), benzoic acid (**H**). Others: 1-phenylacetaldehyde, 1-phenylethane-1,2-diol, benzyl alcohol, phenylglyoxal, and acetophenone. Note: n/a stands for "not applicable".

Table 5. Comparison of the Catalytic Efficiencies of Different Copper(II)−MOF Catalysts with 3 toward the Conversion of Styrene and Selectivity for Benzaldehyde

entry	cat.	solvent	oxidant	temp. (°C)	TOF (h^{-1})	conv. (%)	sel. (%)	refs
1	Cu-Salen-SBA	MeCN	H_2O_2	80	134.6	96.9	45.2	61
2	Cu-SBA-15	H_2O	H_2O_2	100	261.1	84.4	83.9	62
3	Nano-HKUST-1	–	*t*-BuOOH	80	–	92	72[a]	63
4	$[Cu_3(mthd)_2Br]$	MeCN	*t*-BuOOH	80	–	96.4	65.8	64
5	**3**	MeCN	H_2O_2	80	20.7	67.0	100	65
6	$Cu_4(OH)_2(Hppdc)_2(H_2O)_2$	cyclohex	*t*-BuOOH	80	196.0	78.3	60.7[b]	66
7	$Cu_4(OH)_2(Hppdc)_2(H_2O)_2(DMF)$	cyclohex	*t*-BuOOH	80	188.0	75.2	48.9[b]	66
8	SC-TPP-Cu	MeCN	*t*-BuOOH	80	–	93.7	7.70	67
9	FC-TPP-Cu	MeCN	*t*-BuOOH	80	–	72.2	26.4	67
10	Cu-TCPP nanosheets	MeCN	*t*-BuOOH	80	–	94.0	–	68

[a]Yield for benzaldehyde. [b]Epoxide selectivity. Salen = tetradentate C_2-symmetric ligand from salicyladehyde and ethylenediamine; SBA-15 = Santa Barbara Amorphous-15 (or mesoporous silica); HKUST-1 = Hong Kong University of Science and Technology (or $[Cu_3(BTC)_2]$ where BTC is 1,3,5-benzenetricarboxylate); mthd = 2-mercapto-5-methyl-1,3,4-thiadiazole; H_4ppdc = 1-(3,5-dicarboxyphenyl)-2,5-dimethyl-1*H*-pyrrole-3,4-dicarboxylic acid; SC-TPP-Cu = Scholl coupling 5,10,15,20-tetraphenylporphyrin copper; FC-TPP-Cu = Friedel−Crafts 5,10,15,20-tetraphenylporphyrin copper; Cu-TCPP = (4-carboxyphenyl)-porphyrin; cyclohex = cyclohexane; *t*-BuOOH = *tert*-butyl hydroperoxide.

approximately 67% (at 80 °C) (Table S10, entries 1−8). The conversion of styrene shows no obvious optimization as the temperature increases to 90 °C, but the selectivity of benzaldehyde decreases noticeably from approximately 100% (at 80 °C) to 66% (at 90 °C) due to benzaldehyde overoxidation to produce benzoic acid (Table S10, entries 8 and 9). As a result, the optimal reaction temperature was determined to be 80 °C. Furthermore, the effect of different styrene-to-H_2O_2 molar ratios on catalytic performance was investigated. As shown in Figure 6c, as the molar ratios of styrene to H_2O_2 changed from 1:1 to 1:2.75, the conversion of styrene first increased until the molar ratio reached 1:2.5 and then remained constant (Table S10, entries 10 and 11). As the amount of H_2O_2 increases, more •OH radical species are generated, allowing styrene to be oxidized to benzaldehyde (see the mechanism later). Excess H_2O_2, on the other hand, will overoxidize benzaldehyde, producing a benzoic acid byproduct.[52−57] As a result, an optimal molar ratio of styrene to H_2O_2 of 1:2.5 is proposed for efficient styrene oxidation to benzaldehyde conversion. Experiments in various solvents were also carried out. As presented in Figure 6d, the oxidation reaction performed in MeCN displayed substantially higher styrene conversion and benzaldehyde selectivity than the reactions in MeOH and EtOH (Table S10, entries 1−3, 6, and 11).

This is consistent with previous literature reports on styrene oxidation using MeCN as a solvent,[2,6,58−60] which reported 80 °C as the optimum temperature. Entries 12 and 13 (Table S10) demonstrate the catalytic behavior of $[Cu_2(bipy)_2(btec)]$ MOF[32] in various solvents and oxidants, with 100% (H_2O_2) and 26% (*t*-BuOOH) benzaldehyde selectivity. Time extensions of 8, 12, and 24 h significantly reduced both conversion and selectivity toward benzaldehyde and styrene oxide (entries 14−16 in Table S10). Meanwhile, the amount of benzoic acid increased along with other oxidative products. Based on the results of the preceding control experiments, the optimal reaction conditions for maximum styrene conversion are as follows: 0.01 mol % (at approximately 25 mg) of the catalyst, 80 °C reaction temperature, reaction duration of 4 h, a suitable styrene to H_2O_2 molar ratio of 1:2.5, and MeCN as the solvent. Under optimized reaction conditions, the catalytic performances of **1**−**3** in the selective oxidation of styrene to benzaldehyde were systematically assessed. Noteworthy, their respective active catalytic sites are based on dinuclear copper(II) motifs. Compound **3** has the best performance, with approximately 67% styrene conversion and *ca.* 100%

https://doi.org/10.1021/acsomega.3c05999
ACS Omega 2024, 9, 7511−7528

Table 6. Selective Oxidation of Styrene Derivatives by Network 3 to the Corresponding Benzaldehydes[a,b]

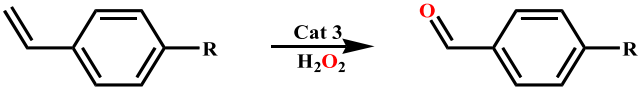

Entry	Substrate	Product	Time (h)	Conv.[b] (%)	Select.[b] (%)
1	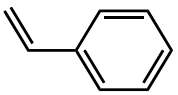	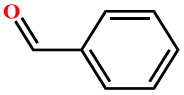	4	67	100
2	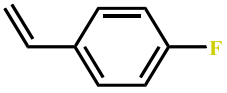	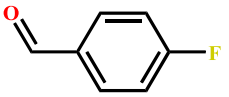	4	57	97
3	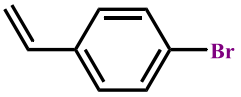	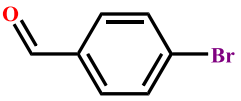	4	59	98
4	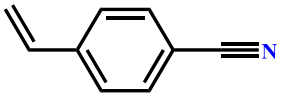	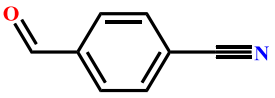	4	56	97
5	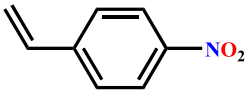	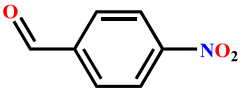	4	58	96
6	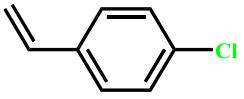	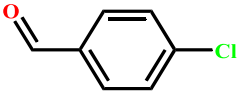	4	61	99
7		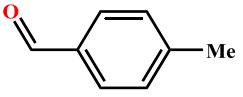	6	64	98
8	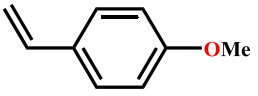	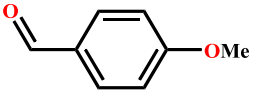	6	66	99

[a]Reaction conditions: styrene (10.0 mmol), catalyst (25 mg, *ca.* 0.01 mol %), molar ratio of styrene to H_2O_2 (1:2.5), and MeCN (15.0 mL) at 80 °C. [b]All values are based on GC-MS spectra.

benzaldehyde selectivity in 4 h (Figure S13 and Table 4, entry 1). Within 4 h, the styrene conversion rate increases with reaction time, while the benzaldehyde selectivity remains constant at 100%. Employing the heterogeneous catalyst **2″**, styrene conversion is *ca.* 59% with the benzaldehyde selectivity of approximately 82% after 4 h (Figure S13 and Table 4, entry 2). Networks **2′** and **1** require 4 h to achieve 54 and 40% styrene conversion with 73 and 69% benzaldehyde selectivity (Figure S13 and Table 4, entries 3 and 4), respectively.

The catalytic performances of **1**, **2′**, and **2″** are inferior to that of complex **3**, with **1** posing as the most catalytically inactive and unstable MOF. The reason could be their low specific surface area, which impedes the accessibility of the reaction substrate to active catalytic channels. Regardless of their identical components, **2″** demonstrated a superior catalytic performance than **2′** because it shows a higher surface area. In general, **1**–**3** possess excellent catalytic performance in the selective oxidation of styrene to benzaldehyde, with the activity order of **3** > **2″** > **2′** > **1**, indicating considerable applicability of framework **3**. A comprehensive comparison of **3** with other known copper-(II)-based MOF catalysts for conversion of styrene and selectivity toward benzaldehyde was carried out, and the results are shown in Table 5. From Table 5, it is evident that catalyst **3** outperforms several other copper(II)-MOF catalysts in terms of benzaldehyde selectivity.

https://doi.org/10.1021/acsomega.3c05999
ACS Omega 2024, 9, 7511−7528

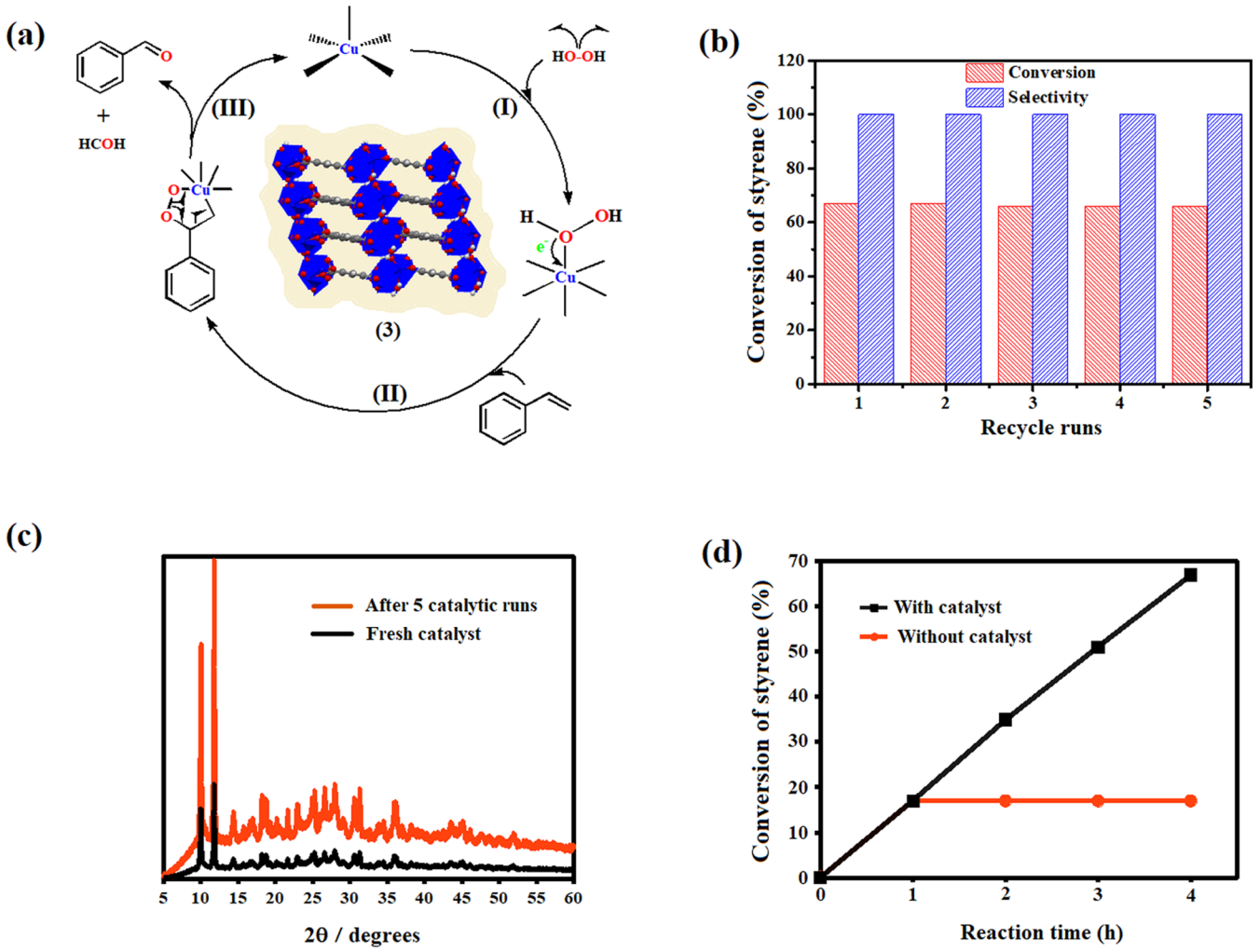

Figure 7. (a) Proposed reaction mechanism of the selective oxidation of styrene with H_2O_2 over catalyst **3** to produce benzaldehyde. (b) Recycling tests with **3** as the catalyst for selective oxidation of styrene. (c) PXRD patterns for catalyst **3** prior (black) and post activation (red) after being used five times. (d) Hot filtration experiment of catalyst **3**.

Moreover, motivated by the excellent catalytic performance of **3** in the oxidation of styrene, the scope of the substrates was broadened to investigate its general applicability. Using **3**, it is evident that substrates with electron-drawing and electron-donating functional groups can be converted smoothly and selectively into their corresponding aldehydes. As illustrated in Table 6 (entries 2−5), 4-fluorostyrene, 4-bromostyrene, 4-cyanostyrene, and 4-nitrostyrene convert between *ca.* 56 and 59% after 4 h of reaction time and demonstrate high aldehyde selectivity. 4-Chlorostyrene was converted after 4 h and showed *ca.* 99% selectivity for 4-chlorobenzaldehyde (**4-Clbenzal**; Table 6, entry 6). It is worth mentioning that the crystallographic data of a new **4-Clbenzal** (refer to Figure S3) polymorph, with CCDC 2274950, is listed in Table S1. Substrates with electron-donating groups, such as 4-methylstyrene and 4-methoxystyrene, require 6 h to achieve approximately 64 and 66% conversions, as well as 98 and 99% product selectivity, respectively (Table 6, entries 7 and 8). In general, the experimental results in Table 6 show that **3**, as a heterogeneous catalyst, possesses good catalytic activity and a relatively rich substrate compatibility, allowing it to catalyze the oxidation of styrene derivatives to the corresponding aldehydes efficiently and selectively.

Based on relevant literature,[65] a tentative reaction pathway (Figure 7a) is proposed for network **3**. The single-electron-transfer cycle between the Cu^{II} and Cu^{I} pair in the SBP $\{CuO_5\}$ active center interacts with H_2O_2 molecule(s) owing to the low diffusion barrier displayed by the catalytic species as well as the accessibility of the paddle-wheel copper dimer.

As in Fenton chemistry,[67−70] oxygen-centered active hydrogen peroxide-derived radicals ($^{\bullet}OH$) and ($\bullet OOH$) are formed. Therefore, the adsorbed styrene interacts with $^{\bullet}OH$ or $^{\bullet}OOH$ to form phenyl hydroperoxyl intermediates, followed by the intermediates converted into styrene oxide and 3-phenyl-1,2-dioxetane on the surface. Subsequently, the active radicals on the interface between the catalyst and the solution mixture continuously oxidize styrene oxide and 3-phenyl-1,2-dioxetane intermediate to produce styrene oxidation products (benzaldehyde as a major scavenger), as described in the literature. The activated catalyst **3** could be recycled five times without a significant loss of activity and selectivity (Figure 7b). As depicted in Figure S14, the TG curve of **3** after being recycled five times (post vacuum drying at 373 K) matches well with that of the as-synthesized fresh catalyst (both exhibit first-step dehydration at 393 K and decomposition at *ca.* 573 K), confirming the heterogeneity and high structural stability of the catalyst. In addition, no noticeable difference is observed in the

https://doi.org/10.1021/acsomega.3c05999
ACS Omega 2024, 9, 7511−7528

PXRD patterns (Figure 7c) of the fresh and recycled catalyst (after being rinsed and vacuum-dried at 373 K for 60 min), indicating the phase robustness of the **3** structure toward the oxidation of styrene in the presence of H_2O_2. As shown in Figure 7d, after the hot filtration of **3** (metal leaching was not detected) from the reaction system, the conversion of styrene in the resulting solution remains unchanged. The lack of change in product conversion and selectivity indicates that catalyst **3** is truly heterogeneous.

Scale-up experiments were conveniently performed to further assess the applicability of this oxidation protocol and, in addition to earlier styrene oxidation products observed, phenol, 1-phenylpropiophenone, and benzyl benzoate were qualitatively identified by GC-MS spectra. In a gram-scale experiment, 6−8 h, 0.20 mol of styrene derivatives, 0.46 g (at 0.15 mol % based on the $\{Cu_2(COO)_4(OH_2)_2\}$ motif) of the catalyst charge, 0.50 mol H_2O_2, and 40 mL of MeCN were sufficient, and benzaldehydes were obtained smoothly in 43−59% yields at 80 °C using a two-necked round-bottom 100 mL flask. This work conveys a possibility to employ this setup in the industrial field.

4. CONCLUSIONS

In summary, a metal−organic framework $[\mathbf{Cu_2(btec)(OH_2)_4}]\cdot\mathbf{2H_2O}$ (**1**) was prepared and thoroughly characterized. The single-crystal structure of **1** was elucidated, revealing a 2D framework with 1D channels and *ca.* 28.3% void. The color change of **1** from blue to light green (**2′**) and dark green (**2″**) upon dehydration at 403 and 433 K, respectively, is attributed to the change in coordination number from five to six. Moreover, the application of heat resulted in SCSC transformations of **1** → **2′** and **1** → **2″**, with the same chemical formula $[\mathbf{Cu_2(btec)}]$, both of which could slowly transform back to **1**. The genuinely reversible **1** ↔ **2′** and **1** ↔ **2″** (low → high symmetry and *vice versa*) transformations were thus clearly established. Essentially, **2′** displayed a maximum water uptake of 0.297 $g\cdot g^{-1}$ at 2−70% relative humidity (RH) and ambient temperature. The water-induced SCSC transformation (*i.e.* **2′** → **3**; $[\mathbf{Cu_2(btec)(OH_2)}]$) was also recognized to be semireversible. Room-temperature inclusion of coordinated water molecules to saturated metal sites of a MOF *via* SCSC fashion is a rare phenomenon. Essentially, it has been shown here that reversibility is seemingly controlled by the size of the crystals and the duration of soakage. Reproducibility and rapidity of the transitions have been rationalized by the single-crystal nature, complete regularity, disparity in framework stability or discrete robust peculiarity, dynamic coordination mode of the linker, as well as the adaptability of Cu(II) coordination geometry. The potential of **3** as a heterogeneous catalyst in the oxidation of styrene, using 30% aqueous hydrogen peroxide as the oxidant, was also illustrated, exhibiting superior performance to **1**, **2′**, and **2″**. Network **3** (showing the smallest Cu···Cu distance of 2.764(14) Å) possesses the highest catalytic activity among the four catalysts investigated, displaying approximately 67% styrene conversion and up to 100% benzaldehyde selectivity within 4 h, with the corresponding TON of 82.6 and TOF of 20.7 h^{-1}. In addition, framework **2′** represents lesser substrate compatibility, recyclability, and structural stability when compared to both **2″** and **3**. Compound **2′** gave TON = 72.4 and TOF = 18.1 h^{-1}, whereas **2″** yielded 73.0 and 18.3 h^{-1}, respectively. Transformation of **2′** to **3** *via* room-temperature (RT) hydration improved the catalytic behavior of this framework, which outperforms most reported Cu(II)-based MOFs as heterogeneous catalysts. Herein, we summarize that the coordinated monohydrate, high surface area along with the accessible metal sites enhanced the catalytic activity of **3**. Ongoing efforts are directed toward finding other frameworks that undergo similar structural transformations upon activation for heterogeneous catalytic oxidation of nonterminal and terminal cyclic olefins, including *para-*, *meta-*, and *ortho-*substituted styrene derivatives among others. This work opens up a new avenue for the development of crystal materials and has significant implications for the recycling of resources. In addition, this study not only presents the structure−property relationship but also provides insight into the design and engineering of an efficient and selective heterogeneous catalyst for essential catalysis applications, particularly in oxidative transformations.

■ ASSOCIATED CONTENT

Supporting Information

The Supporting Information is available free of charge at https://pubs.acs.org/doi/10.1021/acsomega.3c05999.

Tables of crystallographic data, bond lengths, and angles, packing structures, IR spectra, thermogravimetric (TG) and differential scanning calorimetry (DSC) curves, hot-stage microscope (HSM) images, and X-ray diffraction (powder and single-crystal) patterns, including GC-MS (Figures S15−S23) and NMR spectra (Figures S24−S31) (PDF)

SOLVE_3V_a (CIF)

SOLVE_4T_a (CIF)

SOLVE_1S_a (CIF)

SOLVE_3Z_a (CIF)

SOLVE_3P_a (CIF)

SOLVE_3U_a (CIF)

SOLVE_2U (CIF)

SOLVA (CIF)

Accession Codes

CCDC 2206282−2206284, 2206312, 2239239, and 2274950−2274952 contain the supplementary crystallographic data for this paper. These data can be obtained free of charge *via* www.ccdc.cam.ac.uk/data_request/ cif, or by emailing data_request@ccdc.cam.ac.uk, or by contacting The Cambridge Crystallographic Data Center, 12 Union Road, Cambridge CB2 1EZ, U.K.; fax: + 44 1223 336033.

■ AUTHOR INFORMATION

Corresponding Author

Siya T. Hulushe − *Department of Chemistry, Rhodes University, Makhanda 6139, South Africa;* orcid.org/0000-0002-1944-6155; Phone: (+27) 466-038-254; Email: hulushesiya@gmail.com

Authors

Gareth M. Watkins − *Department of Chemistry, Rhodes University, Makhanda 6139, South Africa*

Setshaba D. Khanye − *Division of Pharmaceutical Chemistry, Faculty of Pharmacy, Rhodes University, Makhanda 6139, South Africa*

Complete contact information is available at: https://pubs.acs.org/10.1021/acsomega.3c05999

https://doi.org/10.1021/acsomega.3c05999
ACS Omega 2024, 9, 7511−7528

Author Contributions

S.T.H. conceived, designed, and performed the experiments, analyzed data, and wrote the manuscript; G.M.W. contributed with resources and supervision, reviewed, and edited the manuscript; S.D.K. contributed with resources, reviewed, and edited the manuscript. All of the authors have given approval to the final version of the manuscript.

Notes

The authors declare no competing financial interest.

■ ACKNOWLEDGMENTS

The authors express their gratitude to Professor Rui Werner Maçedo Krause for his assistance with GC-MS/GC data. The authors also thank Dr. Vincent J. Smith for allowing time to utilize the in-house Single-Crystal X-ray Diffraction Facility. Dr. Frederick P. Malan is acknowledged for kindly accepting to evaluate our manuscript, and all of the authors appreciate his insightful comments. Distinguished Professor Leonard J. Barbour and Dr. Alexios I. Vicatos of the Department of Chemistry at Stellenbosch University are sincerely appreciated for conducting the dynamic vapor sorption studies. The authors also thank the anonymous reviewers of the journal whose insightful comments helped them improve the quality of the article. The authors acknowledge the National Research Funding (NRF) of South Africa, Atlantic Philantropies Scholarship, and Rhodes University Research Council for generous financial support.

■ REFERENCES

(1) Otsubo, K.; Nagayama, S. K.; Kawaguchi, S.; Sugimoto, K.; Kitagawa, H. A Preinstalled Protic Cation as a Switch for Superprotonic Conduction in a Metal−Organic Framework. *JACS Au* **2022**, *2*, 109−115, DOI: 10.1021/jacsau.1c00388.

(2) Ponchai, P.; Adpakpang, K.; Bureekaew, S. Selective cyclohexene oxidation to allylic compounds over a Cu-triazole framework via homolytic activation of hydrogen peroxide. *Dalton Trans.* **2021**, *50*, 7917−7921.

(3) Duke, A. S.; Dolgopolova, E. A.; Galhenage, R. P.; Ammal, S. C.; Heyden, A.; Smith, M. D.; Chen, D. A.; Shustova, N. B. Active Sites in Copper-Based Metal−Organic Frameworks: Understanding Substrate Dynamics, Redox Processes, and Valence Band Structure. *J. Phys. Chem. C* **2015**, *119*, 27457−27466.

(4) Fu, L.; Chen, L.; Yuan, H.; Chen, Y.; Li, B. A Two-fold Interpenetrating Metal−organic framework based on $[Co_4O(COO)_6]$ cluster: synthesis, crystal structure and catalytic properties. *Inorg. Chem. Commun.* **2019**, *106*, 180−184.

(5) Kang, S. G.; Kim, K. Y.; Cho, Y.; Jeong, D. Y.; Lee, J. H.; Nishimura, T.; Lee, S. S.; Kwak, S. K.; You, Y.; Jung, J. H. Circularly Polarized Luminescence Active Supramolecular Nanotubes Based on Pt^{II} Complexes That Undergo Dynamic Morphological Transformation and Helicity Inversion. *Angew. Chem., Int. Ed.* **2022**, *61*, No. e202207310, DOI: 10.1002/anie.202207310.

(6) Chen, J.; Chen, M.; Zhang, B.; Nie, R.; Huang, A.; Goh, T. W.; Volkov, A.; Zhang, Z.; Ren, Q.; Huang, W. Allylic oxidation of olefins with a manganese−based metal−organic framework. *Green Chem.* **2019**, *21*, 3629−3636.

(7) Deegan, M. M.; Antonio, A. M.; Taggart, G. A.; Bloch, E. D. Manupilating solvent and solubility in the synthesis, activation, modification of permanently porous coordination cages. *Coord. Chem. Rev.* **2021**, *430*, No. 213679.

(8) Hu, L.; Hao, G.-X.; Luo, H.-D.; Ke, C.-X.; Shi, G.; Lin, J.; Lin, X.-M.; Qazi, U. Y.; Cai, Y.-P. Bifunctional 2D Cd(II)-Based Metal−Organic Framework as Efficient Heterogeneous Catalyst for the Formation of C−C Bond. *Cryst. Growth Des.* **2018**, *18*, 2883−2889.

(9) Cao, L.; Li, Z.; Peng, F.; Wang, W.; Huang, R.; Wang, C.; Yan, J.; Liang, J.; Zhang, Z.; Zhang, T.; Long, L.; Sun, J.; Lin, W. Self-Supporting Metal−Organic Layers as Single-Site Solid Catalysts. *Angew. Chem., Int. Ed.* **2016**, *55*, 4962−4966.

(10) Wang, Z.; Zhu, C.-Y.; Wei, Z.-W.; Fan, Y.-N.; Pan, M. Breathing-Ignited Long Persistent Luminescence in a Resilient Metal−Organic Framework. *Chem. Mater.* **2020**, *32*, 841−848.

(11) Kanagaraj, R.; Jana, A. K.; Babu, P. D.; Siruguri, V.; Maji, P. K.; Panda, S. K.; Paul, A. K. Template-Directed Hierarchical Copper(II)-Organophosphonate Compounds: Syntheses, Crystal Structures, Magnetic and Luminescence Properties. *J. Mol. Struct.* **2021**, *1224*, No. 129027.

(12) Bloch, E. D.; Queen, W. L.; Hudson, M. R.; Mason, J. A.; Xiao, D. J.; Murray, L. J.; Flacau, R.; Brown, C. M.; Long, J. R. Hydrogen Storage and Selective, Reversible O_2 Adsorption in a Metal−Organic Framework with Open Chromium(II) Sites. *Angew. Chem., Int. Ed.* **2016**, *55*, 8605−8609.

(13) Adil, K.; Belmabkhout, Y.; Pillai, R. S.; Cadiau, A.; Bhatt, P. M.; Assen, A. H.; Maurin, G.; Eddaoudi, M. Gas/vapour separation using ultra-microporous metal−organic frameworks: insights into the structure/separation relationship. *Chem. Soc. Rev.* **2017**, *46*, 3402−3430.

(14) Horcajada, P.; Gref, R.; Baati, T.; Allan, P. K.; Maurin, G.; Couvreur, P.; Férey, G.; Morris, R. E.; Serre, C. Metal−organic frameworks in biomedicine. *Chem. Rev.* **2012**, *112*, 1232−1268.

(15) Yan, Y.; Abazari, R.; Yao, J.; Gao, J. Recent strategies to improve the photoactivity of metal−organic frameworks. *Dalton Trans.* **2021**, *50*, 2342−2349.

(16) Kumar, N.; Rom, T.; Singh, V.; Paul, A. K. Transition Metal Ions Regulated Structural and Catalytic Behaviors of Coordination Polymers. *Cryst. Growth Des.* **2020**, *20*, 5277−5288.

(17) Rom, T.; Biswas, R.; Haldar, K. K.; Sarkar, S.; Saha, U.; Paul, A. K. Charge Separated One-Dimensional Hybrid Cobalt/Nickel Phosphonate Frameworks: A Facile Approach to Design Bifunctional Electrocatalyst for Oxygen Evolution and Hydrogen Evolution Reactions. *Inorg. Chem.* **2021**, *60*, 15106−15111.

(18) Zhao, H.-Y.; Li, Y.-Z.; Zhao, J.-W.; Wang, L.; Yang, G.-Y. State-of-the-art advances in the structural diversities and catalytic applications of polyoxoniobate-based materials. *Coord. Chem. Rev.* **2021**, *443*, No. 213966.

(19) Rom, T.; Agrawal, A.; Sarkar, S.; Mahata, P.; Kumar, A.; Paul, A. K. Organoamine Templated Multifunctional Hybrid Metal Phosphonate Frameworks: Promising Candidates for Tailoring Electrochemical Behaviors and Size-Selective Efficient Heterogeneous Lewis Acid Catalysis. *Inorg. Chem.* **2022**, *61*, 9580−9594.

(20) Chakraborty, G.; Park, I. H.; Medishetty, R.; Vittal, J. J. Two-dimensional metal−organic framework materials: synthesis, structures, properties and applications. *Chem. Rev.* **2021**, *121*, 3751−3891.

(21) Xu, M.-Y.; Liang, G.-Y.; Feng, J.-S.; Liang, G.-M.; Wang, X.-J. Temperature-Induced Structural Transformations of Lanthanide Coordination Polymers Based on a Semirigid Tricarboxylic Acid Ligand: Crystal Structures and Luminescence Properties. *Cryst. Growth Des.* **2022**, *22*, 1583−1593.

(22) Sinchow, M.; Konno, T.; Rujiwatra, A. Reversible Structural Transformation and Catalytic Potential of Lanthanide-Azobenzenetetracarboxylates. *Inorg. Chem.* **2022**, *61*, 10383−10392.

(23) Hulushe, S. T.; Watkins, G. M. Guest inclusion of methanol and ethanol in zirconium metal−organic frameworks (Zr-MOFs). *Mater. Today.: Proc.* **2018**, *5*, 10415−10423.

(24) Hulushe, S. T.; Malan, F. P.; Hosten, E. C.; Akerman, M. P.; Lemmerer, A.; Khanye, S. D.; Watkins, G. M. Cation-/Ligand-Induced Solvent-Assisted Transformations of Zn(II) and Cu(II) Complexes Featuring Single-Pocket Multidentate Chelating Members. *Cryst. Growth Des.* **2023**, *23*, 4836−4854.

(25) Zhang, Y. J.; Liu, T.; Kitagawa, S.; Sato, O. Reversible Single-Crystal-to-Single-Crystal Transformation from Achiral Antiferromagnetic Hexanuclears to a Chiral Ferrimagnetic Double Zigzag Chain. *J. Am. Chem. Soc.* **2009**, *131*, 7942−7943.

(26) Dai, F.; Wang, X.; Wang, Y.; Liu, Z.; Sun, D. Sequential solid-state transformations involving consecutive rearrangements of

https://doi.org/10.1021/acsomega.3c05999
ACS Omega 2024, 9, 7511−7528

secondary building units in a metal−organic framework (MOF). *Angew. Chem., Int. Ed.* **2020**, *59*, 22372−22377.
(27) Yan, D.; Chen, Y.; Yang, Y.; Guo, Z.; Guo, J. Single-Crystal-to-Single-Crystal Transformation of Two Copper(II) Metal−Organic Frameworks Modulated by Auxiliary Ligands. *Inorg. Chem.* **2022**, *61*, 1360−1367.
(28) Adhikary, A.; Akhtar, S.; Pariyar, A.; Batsanov, A. S.; Mondal, R. Temperature-Induced Single-Crystal-to-Single-Crystal Transformations with Consequential Changes in the Magnetic Properties of Fe(III) Complexes. *ACS Omega* **2019**, *4*, 8731−8738.
(29) Bravo-García, L.; Larrea, E. S.; Artetxe, B.; Lezama, L.; Gutiérrez-Zorrilla, J. M.; Arriortua, M. I. Structural Transformations in the Thermal Dehydration of $[Cu_2(bpa)(btec)(H_2O)_4]_n$ Coordination Polymer. *Molecules* **2019**, *24*, No. 1840, DOI: 10.3390/molecules24091840.
(30) Brown, K.; Zolezzi, S.; Aguirre, P.; Venegas-Yazigi, D.; Paredes-Garcia, V.; Baggio, R.; Novak, M. A.; Spodine, E. $[Cu(H_2btec)(bipy)]_\infty$: A novel metal organic framework (MOF) as heterogeneous catalyst for the oxidation of olefins. *Dalton Trans.* **2009**, 1422−1427.
(31) Mehlana, G.; Bourne, S. A.; Ramon, G.; Öhrström, L. Concomitant Metal Organic Frameworks of Cobalt(II) and 3-(4-Pyridyl) Benzoate: Optimized Synthetic Conditions of Solvatochromic and Thermochromic Systems. *Cryst. Growth Des.* **2013**, *13*, 633−644.
(32) Cancino, P.; Paredes-Garcia, V.; Aguirre, P.; Spodine, E. A reusable Cu^{II} based metal−organic framework as a catalyst for the oxidation of olefins. *Catal. Sci. Technol.* **2014**, *4*, 2599−2607.
(33) Dale, S. H.; Elsegood, M. R. J. Benzene-1,2,4,5-tetracarboxylic acid at 160 K. *Acta Crystallogr., Sect. E: Crystallogr. Commun.* **2003**, *E39*, o1087−o1088, DOI: 10.1107/S1600536803014351.
(34) Bruker *APEX4, SAINT and SADABS*; Bruker AXS Inc.: Madison, Wisconsin, USA, 2021.
(35) Krause, L.; Herbst-Irmer, R.; Sheldrick, G. M.; Stalke, D. Comparison of silver and molybdenum microfocus X-ray sources for single-crystal structure determination. *J. Appl. Crystallogr.* **2015**, *48*, 3−10.
(36) Bruker *SAINT-Plus*, Version 7.12 (Including XPREP); Bruker AXS Inc.: Wisconsin, USA, 2004.
(37) Bruker *SADABS*, Version 2004/1; Bruker AXS Inc.: Madison, Wisconsin, USA, 1998.
(38) Barbour, L. J. X-Seed − A software tool for supramolecular crystallography. *J. Supramol. Chem.* **2001**, *1*, 189−191.
(39) Sheldrick, G. M. *SHELXL-97*, Program for the refinement of crystal structures; University of Göttingen: Germany, 1997.
(40) Macrae, C. F.; Bruno, I. J.; Chisholm, J. A.; Edgington, P. R.; McCabe, P.; Pidcock, E.; Rodriguez-Monge, L.; Taylor, R.; van de Streek, J.; Wood, P. A. Mercury CSD 2.0 − new features for the visualization and investigation of crystal structures. *J. Appl. Crystallogr.* **2008**, *41*, 466−470.
(41) Cao, R.; Shi, Q.; Sun, D.; Hong, M.; Bi, W.; Zhao, Y. Synthesis and Characterization of Copper(II) Polymeric Complexes Constructed from 1,2,4,5-Benzenetetracarboxylic Acid. *Inorg. Chem.* **2002**, *41*, 6161−6168.
(42) Blackman, A. G.; Schenk, E. B.; Jelley, R. E.; Krensked, E. H.; Gahan, L. R. Five-coordinate transition metal complexes and the value of τ_5: observations and caveats. *Dalton Trans.* **2020**, *49*, 14798−14806.
(43) Bönisch, N.; Maliuta, M.; Senkovska, I.; Bon, V.; Petkov, P.; Platzer, C.; Muller, P.; Kaskel, S. Linker Expansion and Its Impact on Switchability in Pillared-Layer MOFs. *Inorg. Chem.* **2021**, *60*, 1726−1737.
(44) Agterberg, F. P. W.; Kluit, H. A. J. P.; Driessen, W. L.; Oevering, H.; Buijs, W.; Lakin, M. T.; Spek, A. L.; Reedjik, J. Dinuclear Paddle-Wheel Copper(II) Carboxylates in the Catalytic Oxidation of Carboxylic Acids. Unusual Polymeric Chains Found in the Single-Crystal X-ray Structures of [Tetrakis(μ-1-phenylcyclopropane-1-carboxylato-O,O′)bis(ethanol-O)dicopper(II)] and catena-Poly[[bis(μ-diphenylacetato-O:O′)dicopper](μ_3-diphenylacetato-1-O:2-O′:1′-O′)(μ_3-diphenylacetato-1-O2-O′:2′-O′)]. *Inorg. Chem.* **1997**, *36*, 4321−4328, DOI: 10.1021/ic9614733.
(45) Gil-Hernández, B.; Millan, S.; Gruber, I.; Quirós, M.; Marrero-López, D.; Janiak, C.; Sanchiz, J. Improvement of the Proton Conduction of Copper(II)-Mesoxalate Metal−Organic Frameworks by Strategic Selection of the Counterions. *Inorg. Chem.* **2022**, *61*, 11651−11666.
(46) Yang, Y.; Tang, G.; Hu, M.; Shao, L.; Li, J.; Bi, Y. High efficiency synthesis of well-defined cyclic poly(*N*-Vinylcaprolactam) and its solution properties. *Polymer* **2015**, *68*, 213−220.
(47) Shi, D.; He, C.; Qi, B.; Chen, C.; Niu, J.; Duan, C. Merging of the photocatalysis and copper catalysis in metal−organic frameworks for oxidative C-C bond formation. *Chem. Sci.* **2015**, *6*, 1035−1042.
(48) Park, J.; Koo, J. Y.; Choi, H. C. Solvent-Effected Coordination Variation of Flexible Ligands to Cu(II) for the Formation of 1D and 2D Secondary Building Units for Metal−Organic Frameworks. *Inorg. Chem.* **2021**, *60*, 5376−5382.
(49) Du, Z.-Y.; Yu, Y.-Z.; Hong, Y.-L.; Li, N.-F.; Han, Y.-M.; Cao, J. P.; Sun, Q.; Mei, H.; Xu, Y. Polyoxometalate-Based Metal−Organic Frameworks with Unique High-Nuclearity Water Clusters. *ACS Appl. Mater. Interfaces* **2020**, *12*, 57174−57181.
(50) Zheng, Y.; Shen, Q.; Li, Z.; Jing, X.; Duan, C. Two Copper-Containing Polyoxometalate-Based Metal−Organic Complexes as Heterogeneous Catalysts for the C−H Bond Oxidation of Benzylic Compounds and Olefin Epoxidation. *Inorg. Chem.* **2022**, *61*, 11156−11164.
(51) Spek, A. L. Single-crystal structure validation with the program PLATON. *J. Appl. Crystallogr.* **2003**, *36*, 7−13; Structure validation in chemical crystallography. *Acta Crystallogr., Sect. D: Biol. Crystallogr.* **2009**, *65*, 148−155.
(52) Yu, K.; Puthiaraj, P.; Ahn, W.-S. One-pot catalytic transformation of olefins into cyclic carbonates over an imidazolium bromide-functionalized Mn(III)-porphyrin metal−organic framework. *Appl. Catal., B* **2020**, *273*, No. 119059.
(53) Dhakshinamoorthy, A.; Alvaro, M.; Garcia, H. Commercial metal−organic frameworks as heterogeneous catalysts. *Chem. Commun.* **2012**, *48*, 11275−11288.
(54) Rajabi, F.; Karimi, N.; Saidi, M. R.; Primo, A.; Varma, R. S.; Luque, R. Unprecedented selective oxidation of styrene derivatives using a supported iron oxide nanocatalyst in aqueous medium. *Adv. Synth. Catal.* **2012**, *354*, 1707−1711.
(55) Ha, Y.; Mu, M.; Liu, Q.; Ji, N.; Song, C.; Ma, D. Mn-MIL-100 Heterogeneous catalyst for the selective oxidative cleavage of alkenes to aldehydes. *Catal. Commun.* **2018**, *103*, 51−55.
(56) Calmanti, R.; Selva, M.; Perosa, A. Tandem catalysis: one-pot synthesis of cyclic organic carbonates from olefins and carbon dioxide. *Green Chem.* **2021**, *23*, 1921−1941.
(57) Mal, D. D.; Pradhan, D. Selective Oxidation of Styrene on Nanostructured Cerium Vanadate Catalyst. *ACS Appl. Nano Mater.* **2022**, *5* (8), 10441−10451.
(58) Wang, J.-C.; Ding, F.-W.; Ma, J.-P.; Liu, Q.-K.; Cheng, J.-Y.; Dong, Y.-B. Co(II)-MOF: A Highly Efficient Organic Oxidation Catalyst with Open Metal Sites. *Inorg. Chem.* **2015**, *54*, 10865−10872.
(59) Ruano, D.; Díaz-García, M.; Alfayate, A.; Sánchez-Sánchez, M. Nanocrystalline M−MOF-74 as Heterogeneous Catalysts in the Oxidation of Cyclohexene: Correlation of the Activity and Redox Potential. *ChemCatChem* **2015**, *7*, 674−681.
(60) Othong, J.; Boonmak, J.; Ha, J.; Leelasubcharoen, S.; Youngme, S. Thermally Induced Single-Crystal-to-Single-Crystal Transformation and Heterogeneous Catalysts for Epoxidation Reaction of Co(II) Based Metal−Organic Frameworks Containing 1,4-Phenylenediacetic Acid. *Cryst. Growth Des.* **2017**, *17*, 1824−1835.
(61) Yang, Y.; Zhang, Y.; Hao, S. J.; Guan, J. Q.; Ding, H.; Shang, F.; Qiu, P.; Kan, Q. B. Heterogenization of functionalized Cu(II) and VO(II) Schiff base complexes by direct immobilization onto amino-modified SBA-15: Styrene oxidation catalysts with enhanced reactivity. *Appl. Catal., A* **2010**, *381*, 274−281.

https://doi.org/10.1021/acsomega.3c05999
ACS Omega 2024, 9, 7511−7528

(62) Zhu, X.; Shen, R.; Zhang, L. Catalytic oxidation of styrene to benzaldehyde over a copper Schiff base/ SBA-15 catalyst. *Chin. J. Catal.* **2014**, *35*, 1716−1726.
(63) Guo, C.; Zhang, Y.; Zhang, L.; Guo, Y.; Akram, N.; Wang, J. 2-Methylimidazole-Assisted Synthesis of Nanosized $Cu_3(BTC)_2$ for Controlling the Selectivity of the Catalytic Oxidation of Styrene. *ACS Appl. Nano Mater.* **2018**, *1*, 5289−5296.
(64) Zhao, Z.-Q.; Geng, Y.; Song, J.-F.; Cui, X.-B. Cu^I/ Ag^I-containing coordination compounds as advanced catalysts for selective oxidation of styrene to benzaldehyde. *Appl. Organomet. Chem.* **2022**, *36*, No. e6770.
(65) Zhang, A.; Li, L.; Li, J.; Zhang, Y.; Gao, S. Epoxidation of olefins with O_2 and isobutyraldehyde catalyzed by cobalt(II)-containing zeolitic imidazolate framework material. *Catal. Commun.* **2011**, *12*, 1183−1187.
(66) Chen, C.; Shen, P.; Wan, M.; Ding, N.; Shi, X.; Wang, X.; Zhang, N. Size-selective epoxidation of olefins in two new metal−organic framework constructed from six-coordinated tetranuclear Cu(II) SBUs. *Microporous Mesoporous Mater.* **2016**, *232*, 167−173.
(67) Ma, D.; Zhang, Y.; Zhao, H.; Liu, K.; Wang, L. Directing two copper porphyrin based polymers as highly efficient heterogeneous catalysts for styrene oxidation. *Appl. Surf. Sci.* **2022**, *571*, No. 151363.
(68) Xiao, Y.; Guo, W.; Chen, H.; Li, H.; Xu, X.; Wu, P.; Shen, Y.; Zheng, B.; Huo, F.; Wei, W. D. Ultrathin 2D Cu-porphyrin MOF nanosheets as a heterogeneous catalyst for styrene oxidation. *Mater. Chem. Front.* **2019**, *3*, 1580−1585.
(69) Pham, A. N.; Xing, G.; Miller, C. J.; Waite, T. D. Fenton-like Copper Redox Chemistry Revisited: Hydrogen peroxide and superoxide mediation of copper-catalyzed oxidant production. *J. Catal.* **2013**, *301*, 54−64.
(70) Xie, Q.; Wang, Z.; Lei, C.; Guo, P.; Li, C.; Shen, Y.; Uyama, H. Fe-doping induced divergent growth of Ni−Fe alloy nanoparticles for enhancing the electrocatalytic oxygen reduction. *Catal. Sci. Technol.* **2021**, *11*, 5171−5179.

https://doi.org/10.1021/acsomega.3c05999
ACS Omega 2024, 9, 7511−7528